Using Scopesim to Plan Research With the Extremely Large Telescope

Master's thesis
University of Turku
Astronomy
2024
Kristen Gardner
Supervisors:
Dr. Johanna Hartke
Prof. Seppo Mattila
Dr. Hanindyo Kuncarayakti
Examiners:
Prof. Seppo Mattila
Dr. Johanna Hartke

The originality of this thesis has been checked in accordance with the University of Turku quality assurance system using Turnitin Originality Check service.

UNIVERSITY OF TURKU
Department of Physics and Astronomy

Gardner, Kristen Using Scopesim to Plan Research With the ELT

Master's thesis, 84 pp. + Appendix
Physics
September 2024

The python package Scopesim was used to simulate observations with the Extremely Large Telescope. The simulations were used to assess potential research objectives for the ELT. Two case studies were conducted with a set of transient observation simulations: a type Ia supernova and a host galaxy were simulated at varying redshifts, and a supernova progenitor in a star cluster was simulated at varying distances. The simulations were used to analyze the point spread function of the ELT in the K_s, J and Y bands. Difference imaging was used to isolate each target PSF. Strehl ratios were higher at longer wavelengths: 0.55 in the K_s band, 0.22 in the J band, and 0.16 in the Y band. The full-width at half-maximum of the PSF in each respective band was 13.5 mas, 6 mas, and 6 mas, when simulating a 1.5 mas pixel scale. For an exposure time of 1h, the detection limit for a point source is in the range of 26 to 28 mag. Signal-to-noise ratio values were higher at shorter wavelengths, and higher when using a larger pixel scale (4 mas). The PSF was closer to its diffraction limit at longer wavelengths.

Keywords: Adaptive Optics, Scopesim, Extremely Large Telescope, MICADO, Difference Imaging, Transient Astronomy, Astronomy Simulation

Contents

1 Introduction **1**

1.1 The Point Spread Function 1

1.1.1 Diffraction PSF 2

1.1.2 Aberrations 4

1.1.3 Comparison of PSFs 5

1.2 Atmospheric Turbulence and Adaptive Optics 7

1.2.1 Atmospheric Turbulence Parameters 7

1.2.2 Adaptive Optics 8

1.2.3 Wavefront Sensors 10

1.2.4 Guide Stars 12

1.3 The ELT 15

1.3.1 ELT Mirror System 15

1.3.2 MICADO 16

1.3.3 MORFEO 19

1.3.4 Adaptive Optics in the ELT 19

1.4 Supernovae 21

1.4.1 Types of Supernovae 22

1.4.2 Redshift 23

1.4.3 Distant Supernovae 24

1.5 Scopesim 25

1.6 Scopesim Templates 25

2 Simulating MICADO observations with Scopesim **27**

2.1 Input Objects 27

2.1.1 Observing with MICADO and the ELT 29

2.1.2 Star Clusters 30

2.1.3 Stars . . . 31
2.1.4 Galaxies . . . 31
2.1.5 Point Sources . . . 32
2.1.6 Source From File . . . 33
2.2 Carrying Out Observations . . . 33
2.2.1 SCAO vs MCAO . . . 34
2.2.2 The Pixel Scale and Field of View . . . 34
2.2.3 Environmental Parameters and Telescope Pointing . . . 36
2.2.4 Photometric Filters . . . 38
2.3 Empty Sky Calibration . . . 39

3 Metrics For Analyzing the PSF 41
3.1 Intensity Cross-Section of a Point Source Image . . . 41
3.2 The Strehl Ratio . . . 44
3.2.1 Airmass . . . 45
3.3 Signal-To-Noise Ratio . . . 47

4 Observing a Supernova and a Galaxy 48
4.1 Angular Resolution . . . 50
4.2 Observation Results . . . 52

5 Observing a Supernova Progenitor and a Star Cluster 56
5.1 Results . . . 59
5.1.1 Detection Limit . . . 61

6 Discussion 63
6.1 Procedure Summary . . . 63
6.1.1 Scopesim Templates . . . 63
6.1.2 Introducing Analysis Tools . . . 65

6.1.3 Supernovae And Galaxies 66
6.1.4 Supernovae Progenitors and Star Clusters 67
6.2 Analysis 68
6.2.1 The FWHM, Strehl Ratio, and SNR 68
6.2.2 Comparison With Other Telescopes 70
6.2.3 Use of Multiple Exposures and Positions 74
6.2.4 Difference Imaging 75

7 Conclusion **76**

A Derivation Of The Airy Disk **85**

1 Introduction

The Extremely Large Telescope (ELT) is currently under construction. When completed, it will be the largest, most advanced optical and infrared telescope ever created. It will be capable of providing images 15 times sharper than images from the Hubble Space Telescope, and will collect more light than all of the 8-10-meter telescopes currently in operation. The ELT will make use of an advanced adaptive optics (AO) system to maximize its potential for resolving faint objects. With the ELT, it will be possible to observe fainter, more distant objects than ever before.

In preparation for the opportunity to utilize this new technology, researchers are studying the ELT's optical system, to plan future research as realistically as possible. Computational simulations can provide a detailed depiction of possible observational data.

The purpose of this research is to gain a realistic first impression of observational data from the ELT, to determine the feasibility of various observational objectives. The primary topic that is considered in this research is highly redshifted, distant supernovae.

1.1 The Point Spread Function

A point spread function (PSF) describes the intensity of light across a focal plane after the light emitted from a point source has been transformed by an optical system. The PSF is an indication of an optical system's ability to resolve details in an image. The more narrow a point spread function is, the higher the resolution of the optical system. The sharpness of the PSF is determined by the diffraction limit and aberrations of the system [1].

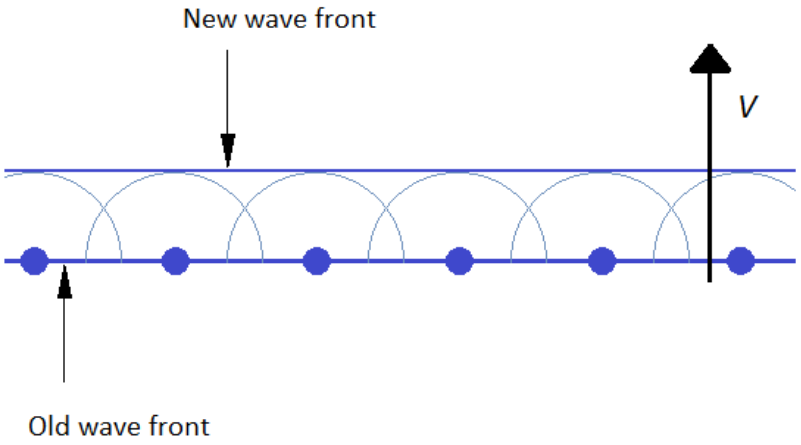

Figure 1: Huygens's Principle: Each point on a wavefront is the source of a spherical wavelet. (Created by the author)

1.1.1 Diffraction PSF

According to Huygens's Principle, each point on a wavefront can be considered a point source, where a spherical wavelet is emitted [2]. A plane wave that is unbridled by any aperture will continue to propagate as a plane wave, because the sum of the spherical wavelets is still a plane wave, as shown in Figure 1.

Light that passes through an aperture will display a diffraction pattern. The sum of the limited set of wavelets will interfere constructively and destructively in different directions [2]. Light waves are in phase when passing through the aperture. When they propagate at an angle θ they will have different path lengths, and will converge on the image plane in different phases. If the path difference between two wavelets is a multiple of their wavelength, they have maximum constructive interference; if the path difference is an odd multiple of half the wavelength, the wavelets have maximum destructive interference. The sum of all wavelets passing through the aperture is maximally destructive if the wavelet at the center of the aperture is out of phase with the wavelets at the edge of the aperture. For an

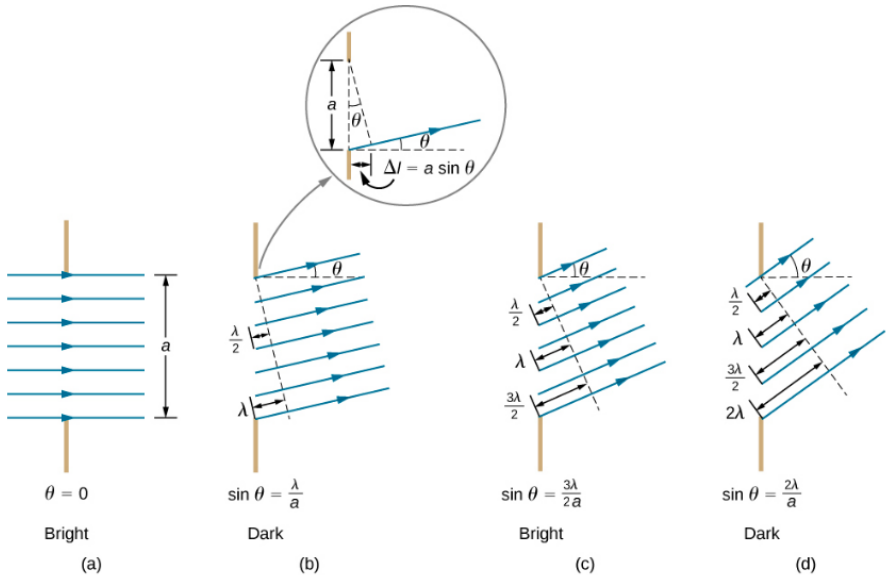

Figure 2: Single slit diffraction through an aperture of width a. The apparent intensity of light is dependent on the angle of the rays. Figure from [3]

aperture with a width a, and a plane wave with a wavelength of λ, the angle of maximum destructive interference θ can be found with the equation $a \sin\theta = m\lambda$. This concept is summarized by Figure 2.

For a circular aperture, the interference pattern appears as a bright central area, with alternating rings of light and dark. This pattern is called the Airy disk, and is shown in appendix A, in Figure A3b. The width of the Airy disk is the minimum area in which the light from a point source can be focused. The diffraction limit of a system determines the minimum distance needed between two point sources such that the Airy disk patterns are distinguishable. The angular radius of the Airy disk θ for a wavelength λ and an aperture diameter D is

$$\theta = \sin^{-1}\left(\frac{1.22\lambda}{D}\right). \tag{1}$$

The mathematics describing the size of the Airy disk is considerably more complicated than that of a thin rectangular aperture. To examine this diffraction pattern more thoroughly, refer to appendix section A.

The wave nature of light guarantees that a point source image will have a finite angular size, and limit the resolution of an image. We require larger telescopes to increase the resolution of our observations. No other design improvements for a single telescope that will be able to decrease the area of an Airy disk and the diffraction limit. A perfectly designed optical system with no flaws or aberrations of any kind would not be able to resolve two points within the diffraction limit of the telescope [4].

1.1.2 Aberrations

An optical aberration is any distortion of an image in the focal plane of an optical system caused by limitations or flaws of that system. Aberrations can be described with ray-tracing (geometric optics).

Spherical aberration is a common problem in reflecting telescopes. A spherical mirror with a small radius, relative to its radius of curvature, makes a decent approximation of a parabolic mirror. Spherical surfaces rely on a small-angle approximation for calculating a single focal point for multiple parallel rays. The farther away the approaching rays are from the optical axis, the more they will diverge from the calculated focal point, as shown in Figure 3a. To avoid spherical aberrations, a parabolic mirror is needed. Spherical mirrors are still more common than parabolic mirrors, because spherical surfaces are easier to manufacture [5].

Comatic aberration is an off-axis aberration; it occurs in light rays that are not parallel to the optical axis. When comatic aberration is present, parallel rays that reflect off of the mirror at points that are equidistant from the center of the mirror will form an off-centered circle on the image plane. For greater distances from the center of the mirror, the circle is larger, and centered farther from the image point. This results in a point-source appearing to have a cone shape. This aberration is also present in optical systems with spherical lenses. The geometry of comatic aberration

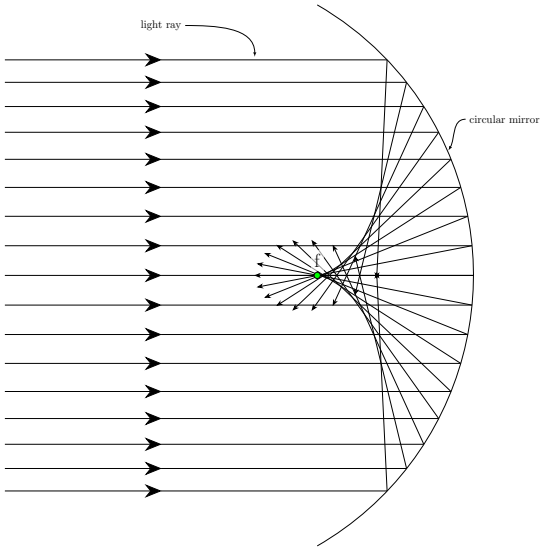

(a) A diagram of spherical aberration in a mirror. (Created by the author)

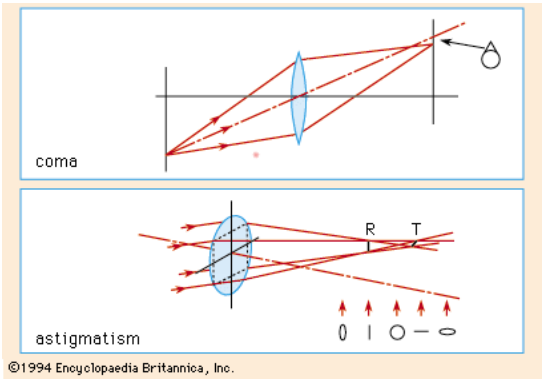

(b) Diagrams of comatic aberration and astigmatism. Figure from [6]

Figure 3

is shown in Figure 3b.

Astigmatism is another off-axis aberration, where tangential and sagittal rays have different focal lengths. For an off-axis object, the chief ray (the ray passing through the object and the center of the aperture) and the optical axis define the tangential plane. The sagittal plane is perpendicular to the tangential plane. Rays in each of these planes have different focal lengths when the chief ray has a wide angular separation from the optical axis. This aberration can also occur on-axis if the mirror or lens has different radii of curvature in different planes. The geometry of astigmatism is shown in Figure 3b.

1.1.3 Comparison of PSFs

The resolution of an optical system depends on its PSF. The narrower the PSF, the closer two separate point sources can be to each other and still be resolved.

The full width at half-maximum (FWHM) is a value that indicates the overall width of a normal distribution. For a distribution with a central maximum that

decreases with increasing distance from the center, the FWHM is the distance between points on either side of the center where the value of the distribution function is equal to half of the central maximum. The FWHM is useful for judging the width of non-uniform distributions. Instead of including the complexities of the distribution's shape, the FWHM is an option for reporting the width of a distribution with a single numerical value [7].

Another way to measure the quality of an optical system is to find the Strehl ratio of the PSF. The Strehl ratio is the ratio of the maximum light intensity of an aberrated PSF, to the maximum light intensity of an ideal, unaberrated PSF [8]. If the light in a PSF is spread across a wider area than the Airy disk, the peak intensity of the PSF must be lower than the peak intensity of the Airy disk, so that the real and ideal versions of the PSF contain the same total quantity of light. A higher Strehl ratio means that a PSF is narrow and close to the diffraction limit; a low Strehl ratio indicates that a system heavily affected by aberrations and has a low resolution for its aperture size. One way to calculate the Strehl ratio of a point source image is to calculate the Airy disk diffraction pattern across an array, for the same wavelength and pixel scale as the PSF image. This diffraction pattern must then be normalized to the same total flux as the PSF. The ratio of the central peak of the PSF and the central peak of the Airy disk is the Strehl ratio of the PSF.

1.2 Atmospheric Turbulence and Adaptive Optics

The quality of an observation through a ground-based telescope is not only limited by diffraction and optical aberrations, it is limited by atmospheric seeing. The light from astronomical sources must pass through the Earth's atmosphere before being observed with the ELT. Light passing through different areas will be refracted in slightly different directions, depending on localized atmospheric conditions. The atmosphere is turbulent; the refractive properties of any given optical path are constantly changing with the changes in local air currents. Thus, it is very challenging to reduce the effects of atmospheric interference. Modern ground-based telescopes use AO to correct the distortions caused by the atmosphere. The ELT will have a unique, advanced AO system, allowing the high spatial resolution of ELT to be actualized.

1.2.1 Atmospheric Turbulence Parameters

There are three parameters describing the properties of atmospheric conditions that must be measured for the successful implementation of AO [9].

The Fried Parameter (r_0) relates to the width of the turbulent cells and their effect on the wavefronts. Specifically, r_0 is defined as the length over which the wavefront changes phase by 1 radian. This length is dependent on both the atmosphere itself, as well as the wavelength being observed, with the relation $\mathrm{r}_0 \propto \lambda^{\frac{6}{5}}$. The Fried Parameter determines the necessary complexity of the AO system, i.e. the number of lenslets in the wavefront sensor and mirror segments in the deformable mirror. Having a larger fried parameter is ideal because the AO correction is effective across a wider area, for a longer period of time. Because of the relation between r_0 and the wavelength, AO corrections are easier to achieve in the infrared range of the spectrum than in visible light.

Coherence time t_0 describes the temporal variance in the optical distortion. The

velocity v of the wind at the altitude of the turbulent cells moves a cell across a distance equal to its own length in a time $t_0 \propto \frac{r_0}{v}$ with t_0 being the coherence time. This time is generally on the order of milliseconds for visible light. It is essential for the time between wavefront detection and mirror adjustment to be less than the coherence time. Slower adaptations will not be correct for the interference of turbulence in the present moment. Because the coherence time is proportional to the Fried parameter, and the Fried parameter is related to the wavelength as $r_0 \propto \lambda^{\frac{6}{5}}$, the coherence time is also longer for observations of longer wavelengths. AO corrections can be made more slowly when observing in the infrared, and are therefore easier to utilize successfully. For example, in the K_s band, with a central wavelength of 2.16μm, the coherence time is 5$\times$ longer than in the green band, with a wavelength of 565 nm.

The isoplanatic angle Θ_0 is the angular width across an area in the sky in which an AO correction is accurate. This angle relates to the Fried Parameter by $\Theta_0 \propto \frac{r_0}{H}$ where H is the distance between the turbulence and the telescope. Effective AO corrections are easier to achieve with a larger isoplanatic angle. Figure 4 depicts a set of turbulent cells in the atmosphere, the Fried Parameter in a particular area, the corresponding isoplanatic angle, and a velocity vector. Two stars are located within the isoplanatic angle, behind one turbulent cell. The cells are moving with a velocity to the left. After the coherence time t_0 passes, a new turbulent cell will be in-between these stars and the telescope, and a new AO correction will need to be made. A third star on the right must be viewed with a different correction than the two on the left.

1.2.2 Adaptive Optics

AO is a method of correcting optical degradation in an astronomical observation caused primarily by turbulence in the atmosphere, and secondarily by vibrations in

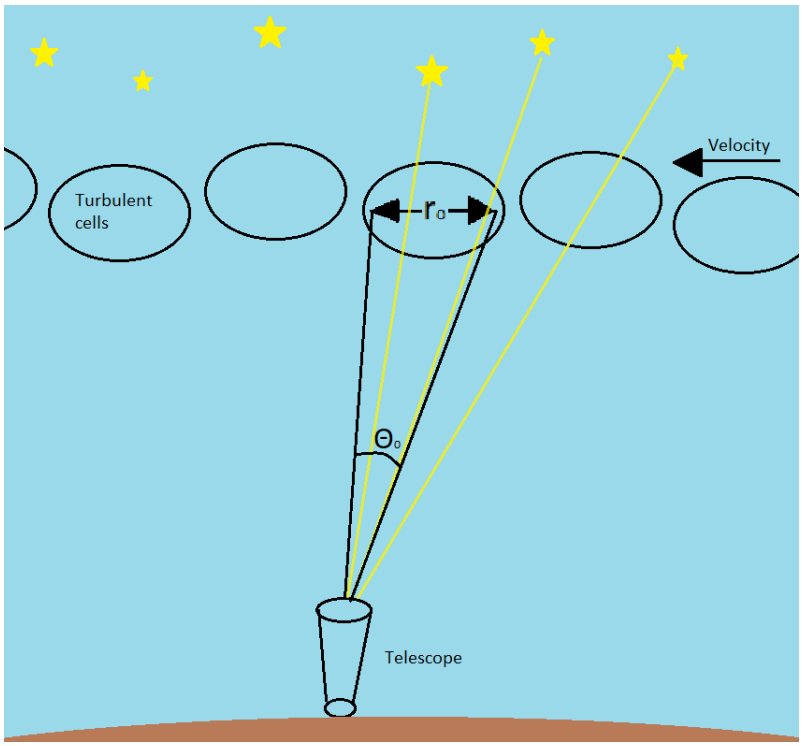

Figure 4: A diagram of stars being observed from behind a set of turbulent atmospheric cells.(Created by the author)

the telescope. The main components of an AO system in a telescope are a wavefront sensor, a deformable mirror, and a high speed computer.

Light rays from a distant point source approach Earth as a plane wavefront. The wavefront sensor monitors the deformation of waves of incident light. Data from the wavefront sensor is used to calculate the corrections that must be made by the deformable mirror, to restore the deformed waves to plane waves. This information is sent to the deformable mirror, which makes rapid changes across its surface to counteract the detected wave deformations.

Making these corrections requires understanding the general form of air currents above a telescope. Turbulent airflow in the atmosphere consists of moving cells of air, with similar indices of refraction inside the cell, and different indices of refraction outside. Within each cell, the refraction of the wave is similar, and the wavefront remains approximately planar. The original wave is essentially broken into multiple plane waves of smaller area. The area of these new wavefronts is determined by the size of the turbulent cells. Ideal observing conditions are characterized by larger cells, and therefore fewer distortions.

1.2.3 Wavefront Sensors

Wavefront sensors are a necessary component of any AO system. They are used to measure the phase and amplitude of incoming light to an optical aperture, from a distant point source. In an ideal system, light from a distant point source is received as homogeneous plane waves. Heterogeneity of wavefronts is caused by disturbances in the optical path. These distortions are identified and corrected using data obtained from wavefront sensors. This section discusses three general types of wavefront sensors used in optical systems.

One of the types of wavefront sensor typically used in AO, and the type used by the ELT, is the Shack-Hartman wavefront sensor (SHWFS). A SHWFS uses a

lenslet array: a grid of identical tiny lenses that each focus incident light onto a charge-coupled device (CCD) or an infrared detector. An undistorted plane wave would yield a uniform grid of point source images on the focal plane. The wavefront distortions cause the light from each wavelet to propagate in slightly different directions. The resulting image on the detector consists of points that are misaligned from the ideal uniform grid. The positions of each point are used to calculate the corrections that must be made by the deformable mirror [10–12].

Another type of wavefront sensor is the lateral shearing interferometry (LSI) type. A LSI sensor uses a diffraction grating to split the wavefront into four identical adjacent waves. A few millimeters beyond the grating, the waves interfere with each other and form an interferogram on a CCD detector. The nature of the deformation of these identical waves is revealed in the interference pattern captured by the detector, so that corrections can be made by the deformable mirror [12, 13].

The SHWFS is ideal for AO because it is a simple, compact, robust system that allows rapid real-time calculations. The main disadvantages of the SHWFS are that the spatial resolution is limited by the size and quantity of lenslets, and that it must operate with a specific wavelength to maintain accuracy. The LSI sensors can provide higher-resolution data, and use a range of wavelengths. However, the LSI is an undesirably complex, heavy, bulky system, with a high sensitivity to microvibrations.

One type of wavefront sensor that will be used by the ELT is the pyramid wavefront sensor (PWS) [14]. A PWS uses a pyramidal prism to split a wavefront into separate beams. The apex of the pyramid is placed in the image plane of the system, where the wavefront converges [15]. For a wavefront that is free of aberrations, the pyramid would split the beam into four identical beams, which are then focused by a relay lens, and projected as four identical images on a detector [16]. With aberrations, the refraction of the wavefront through a surface of the

pyramid will vary, causing the resultant images to be different. The refraction of light through a pyramid face from any given direction will depend on the gradient of the wavefront through that optical path. The gradient of the wavefront can be determined by measuring the discrepancies in light distribution between each of the images [17].

A PWS often requires modulation of either the pyramid itself, or the light beam, to ensure that the light beam spends equal amounts of time at each surface of the pyramid. This can be accomplished with a tip-tilt mirror, which can rapidly modulate the path of the beam around the center of the pyramid, or by rapidly vibrating the pyramid about the optical axis [15]. This allows the beam to refract through each face of the pyramid evenly. While pyramid wavefront sensors are generally disadvantaged by a need for moving parts, they are highly sensitive and yield very accurate wavefront measurements, making them ideal for high-resolution imaging [18, 19].

1.2.4 Guide Stars

AO requires the presence of a "guide star" within the isoplanatic angle of the observation target. A guide star is a bright point source that can be reliably observed at very short exposure times. The target itself can potentially serve as a guide star, but observations are often made of faint objects that require much longer exposure times than the AO coherence time. A natural guide star can be used, if a bright star happens to be close to the target. However, this is not an option throughout much of the sky [20].

A more reliable method of using a guide star for any target in the sky is to generate one using laser beams; this is known as a laser guide star. The main advantages of using a laser guide star are that they can be placed anywhere in the sky, and they can have any desired brightness. A few disadvantages are: laser beams

experience some distortion when they travel from the telescope to the sky, and are therefore less precise point-sources, there is significant cost and difficulty to building and using high powered lasers, there are safety concerns for any aircraft flying near the beams, and laser guide stars cannot be used to detect tip-tilt of the telescope.

Laser guide stars fall into two categories. Sodium beacons are guide stars that are made using lasers that have a wavelength of 589.0 nm. This wavelength interacts with a layer of sodium in the upper atmosphere, at an altitude of about 90km. This wavelength is absorbed by the Na I D2 transitions, and is then re-emitted. The result is the appearance of a point source 90km above the Earth's surface [21]. The Rayleigh beacon is made with a laser that causes Rayleigh scattering in the lower atmosphere, at about a 20km altitude [22]. This beacon slightly less advantageous because the guide star appears much lower in the atmosphere, and may not experience the full extent of the turbulence that a point source from a higher altitude would. Most of the turbulence, however, exists in the troposphere: the lowest layer of the atmosphere. The top of the troposphere ranges from 6 km to 20 km. Beyond the troposphere, air is no longer moved by convection, and movement is generally much less turbulent. Figure 5 depicts the relative locations of different laser guide stars and atmospheric turbulence [23, 24].

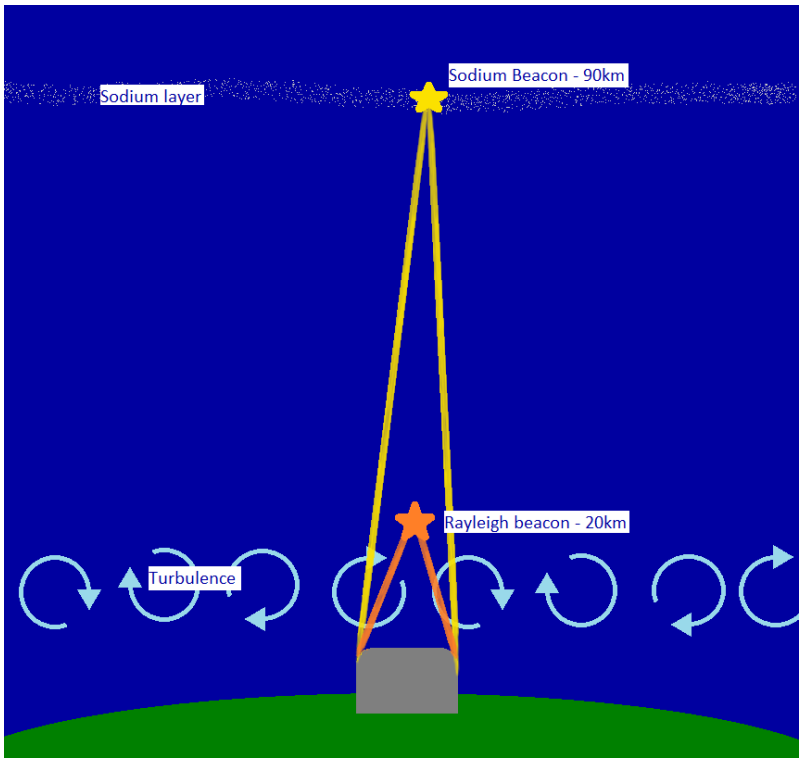

Figure 5: A diagram of laser beams generating a sodium beacon at an altitude of 90km, and a Rayleigh beacon at an altitude of 20km. Atmospheric turbulence is shown below the Rayleigh beacon.(Created by the author)

1.3 The ELT

The ELT is a near-infrared and optical astronomical telescope that is currently under construction at the top of Cerro Armazones, in Chile. When completed, it will be the largest optical and infrared telescope in the world. The ELT is part of the European Southern Observatory (ESO).

The selection of Cerro Armazones as the site of this telescope was the conclusion of a thoughtful and extensive investigation. This mountain is located in Chile's Atacama Desert, with an altitude of 3046m, a median relative humidity of 15%, and annual rainfall of the order of 100 mm [25]. The location is ideal for astronomical observations with minimal environmental interference. The site was selected by the ESO in 2010, and an agreement was made between the ESO and the Chilean government in 2011. Construction began at Cerro Armazones in 2014. The ELT is expected to be ready for technical first light in 2028 [26].

1.3.1 ELT Mirror System

The ELT will consist of a 5-mirror system, as shown in Figure 6. The primary mirror will be 39.3 m wide and have a 68.7 m radius of curvature. This mirror will be comprised of 798 mirror segments, acting as a single mirror [27].

The secondary mirror is a 4.25 m convex mirror, with an 800 mm central hole. It will reflect light received from the primary mirror, to the third mirror. The tertiary mirror is a 4 m concave mirror, with a 30 mm central hole [28].

The quaternary mirror is a 2.4 m wide deformable mirror. It is an essential component of the ELT's AO system, and the largest mirror of its kind. The deformable mirror will compensate for atmospheric turbulence, and vibrations of the telescope itself, by making up to 1000 adjustments to its surface each second. The surface of the mirror will be made of six segments of thin ceramic glass. The glass acts as a malleable membrane, which is manipulated by about 5000 voice coil actua-

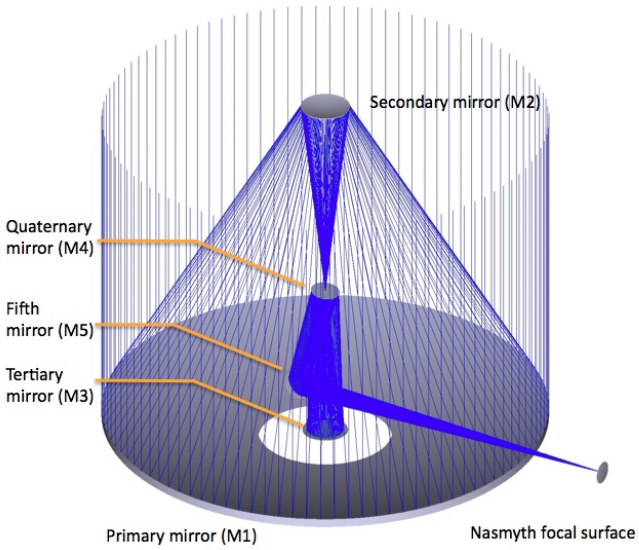

Figure 6: A diagram of the ELT mirror system. Figure from [31]

tors. The actuators use a permanent magnetic field and dynamic electric currents to create high-speed, precise movements. The adaptive properties of this mirror will drastically increase the resolution of the telescope [29].

The quinary mirror is a flat, elliptical mirror that is 2.7m by 2.2m. It is also an important component of the AO system. This mirror will make precise adjustments to its tip and tilt angles to correct any image movements caused by wind and vibrations of the telescope itself. It was designed to be very lightweight and rigid, so it could make these adjustments with a spatial accuracy of tens of milli-arcseconds, and temporal accuracy of tenths of a second [30].

1.3.2 MICADO

MICADO (Multi-AO Imaging Camera for Deep Observations) is one of the instruments that will be utilized with the ELT, and is the instrument that was simulated in this research. It is an infrared camera that – when combined with the ELT – has six times the spatial resolution of the James Webb Space telescope. MICADO will work with the ELT's wide mirror system and advanced AO system to provide images of the distant universe with unprecedented detail. It can use a coronagraph to block

bright light sources, allowing observations of other, much fainter objects, such as exoplanets. As an extremely precise infrared camera, MICADO will be housed in a cryostat, to prevent interference from ambient thermal radiation [32].

MICADO has two filter wheels and a pupil wheel, with several options for filtering light: *IYJHK* broad band filters, and medium and narrow band filters. MICADO images will have relative astrometric accuracy 50 μas. There will be two options for the field of view: 50.5"x50.5" (4mas pixels) and 18"x18" (1.5mas pixels). The MICADO single-slit spectrometer will cover a wavelength range of 0.84-2.46μm over two exposures, with one exposure covering the range 1.45-2.46μm, and another covering the range 0.84-1.48μm. The dimensions of the spectrograph's slit are 16mas and 3arcsec [32].

Figure 7 shows the main components of MICADO. The MICADO calibration assembly (MCA) will assist in multiple calibrations. The MCA will offer

- flat-field calibration using a tungsten bulb
- wavelength calibration using multiple sources of emission spectra
- astrometric calibration using a set of miniature tungsten bulbs behind a reference target mask that yields point-sources through a set of pinholes
- moving source calibration, using a movable point source to calibrate the Single Conjugate Adaptive Optics (SCAO) system for non-sidereal observations [33].

The relay optics (RO) receives light from the telescope, or the MCA, and directs it into the "Green Doughnut" structure. This area contains the SCAO wavefront sensor (WFS) and the Multi-Conjugate Adaptive Optics (MCAO) natural guide star low order and reference (LOR) WFS; this is where the effects of atmospheric turbulence are recorded [34]. The light is then sent through the focal plane mask wheel and aperture wheel: which contain the field stops, slits, coronagraphs and calibration mask [35]. The collimator makes the light rays parallel, before sending

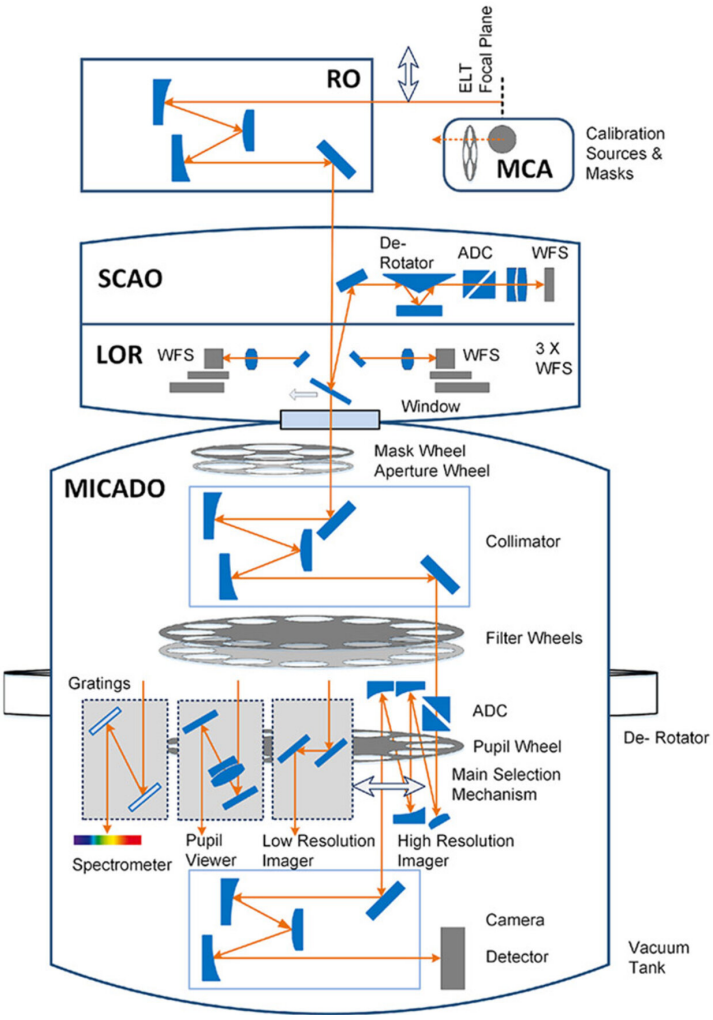

Figure 7: A diagram of the MICADO camera. Figure from [32]

the light to the atmospheric dispersion corrector (ADC) and the filter wheels. The filter wheels contain a set of photometric filters, which will transmit only the desired portion of the spectrum. After the light has been filtered, it is directed to one of four optical components at the end of the optical path, either: the spectrometer, the pupil viewer, the low resolution imager, or the high resolution imager. The spectrometer is selected if a spectrum is being observed. The pupil viewer is used for testing and checking the functionality and alignment of MICADO in the ELT. The detector is used to record the signal.

1.3.3 MORFEO

The AO instrument MORFEO (Multi-conjugate adaptive Optics Relay For ELT Observations) is part of the ELT's MCAO system. It will not make any observations on its own; it will work with MICADO for optimal imaging. It has been designed to also work with a new spectrograph in the future. MORFEO will use three deformable mirrors, and nine guide stars: three natural guide stars and six laser guide stars. It will make AO corrections for turbulence at three altitudes [36].

1.3.4 Adaptive Optics in the ELT

The ELT will utilize multiple AO modes. MICADO will be able to use SCAO and MCAO (Figure 8).

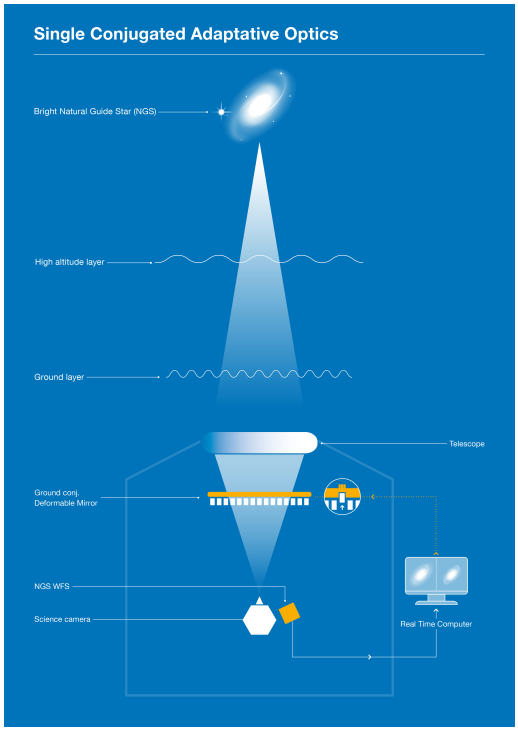

(a) A diagram of the SCAO system. Figure from [37]

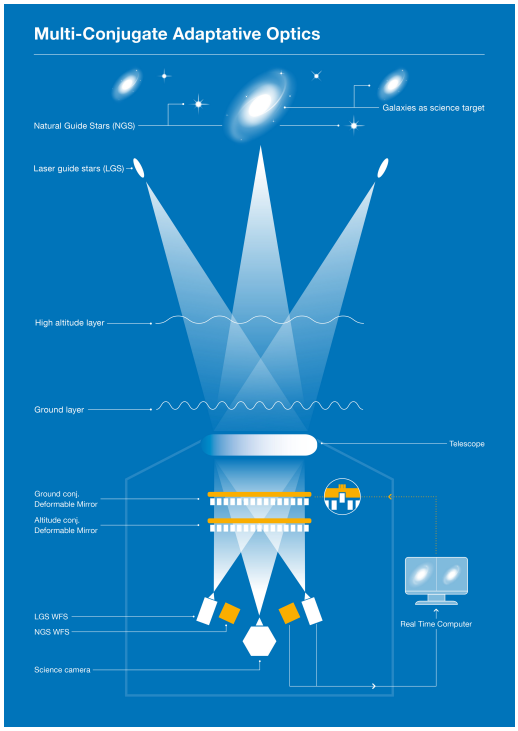

(b) A diagram of the MCAO system. Figure from [37]

Figure 8

Multiple guide stars or a single guide star can be used in an observation. SCAO uses a single natural guide star to correct for turbulence in a small area around the guide star. This method is effective, but limits an observation to a narrow field of view. A more sophisticated approach is MCAO, which uses multiple laser guide stars, multiple natural guide stars, and multiple wavefront sensors, to measure interference in several directions, and make corrections over a wider area. Tomographic reconstruction is used to process multiple distorted wavefronts, estimate 3D turbulence, and make corrections with multiple deformable mirrors. The ELT instrument MORFEO contains additional deformable mirrors, which work with MICADO to utilize MCAO [37].

The ELT will also use Ground Layer Adaptive Optics (GLAO) with the instrument MOSAIC, a multi-object spectrograph. This mode makes corrections for turbulence at the ground level, using multiple wavefront sensors. The ground level turbulence is uniform across the telescope's field of view, so this correction is effective across the entire image [37].

Laser Tomography Adaptive Optics (LTAO) uses multiple wavefront sensors to analyse the center of the field-of-view, and makes corrections with only one deformable mirror. LTAO is essentially a compromise between SCAO and MCAO. It will be utilized with the spectrograph HARMONI [37].

Implementing AO in the ELT entails greater challenges than its implementation in smaller telescopes. Having a primary mirror with such a large area means that a greater area across the atmosphere will contribute to the distortions. A larger area will have a greater quantity of turbulent cells, which will be present in the observations. These turbulent cells, and the high resolution of the telescope, require higher order corrections to be made, to allow the resolving power of the telescope to be actualized [38, 39]. Higher order corrections require more advanced mechanical and computational systems. A greater number of actuators are needed in the

deformable mirror, to increase the complexity of deformations. These additional actuators must all be tightly controlled, move rapidly, and coexist in a small area. High order corrections require sophisticated algorithms, and a large amount of computational power; corrections must be computed rapidly, and large amounts of data must be transferred to the deformable mirror [40].

The ELT has multiple AO systems with multiple deformable mirrors, wavefront sensors, and laser guide stars. These multiple systems must coexist harmoniously within the greater ELT system. The added complexity of these many components make it challenging to design an ELT system. Coordinating the use of these AO systems make observations with the ELT a more sophisticated endeavor. These complexities also necessitate excellent design and manufacturing of ELT components. Parts must be robust, and work flawlessly for long periods of time. Regular maintenance will also be necessary to ensure the continued functionality of the ELT.

1.4 Supernovae

A supernova is a bright, transient astronomical event that occurs when a star becomes unstable and explodes. During a supernova, a star releases an extremely large amount of energy and mass; a star from beyond the local universe can become bright enough to be observed by astronomers. The physical characteristics and elemental composition of the dying star determine the spectral and photometric properties of the supernova [41]. Every extragalactic supernova provides astronomers with an opportunity to learn about the galaxy in which the supernova occurs [42, 43]. Humanity's ability to observe and study very distant supernovae is limited by the quality of our telescopes. With the ELT, astronomers endeavor to expand their horizon of supernova observation, and study the properties of the distant universe.

1.4.1 Types of Supernovae

Some stars will experience a supernova when their internal pressures can no longer counteract their gravitational force. The two general ways that a supernova occurs depend on the main force that had been resisting gravity within the star.

White dwarf stars are small, dense stars that have ceased nuclear fusion. They resist collapse through electron degeneracy pressure [44]. If a white dwarf star accretes mass from a companion star, its mass can increase until it reaches the Chandrasekhar limit: the mass limit of a white dwarf star, beyond which, electron degeneracy pressure cannot sustain the star's structure [45]. This sudden collapse results in a type Ia supernova. This type of supernova occurs with a relatively consistent quantity of mass, and therefore it has a consistent luminosity. Type Ia supernovae serve as an indicator for the distance of the galaxy they are located in [46, 47].

More massive stars experience a supernova when nuclear fusion no longer yields the necessary pressure to resist gravity. Stars with a mass of at least 8 solar masses will fuse heavier and heavier elements throughout the course of their life, until they reach iron [48, 49]. The fusion of iron into heavier elements would require more energy than is released by the reaction. When this limit is reached, a star can no longer resist the inward pressure of gravity. The star's core rapidly collapses, until either a neutron star or a black hole is created, and the remaining mass is expelled from the system. These supernovae can occur with a wide range of stellar masses, and a diverse set of elemental compositions. Depending on these properties, they can be classified as type Ib or Ic if hydrogen absorption lines are absent from their spectra, or any subcategory of type II if hydrogen lines are present [50, 51].

1.4.2 Redshift

When observing distant objects, its important to consider the redshift of the object's light curve. Distant objects are moving away from the Milky Way due to the expansion of the universe. The more distant an object is, the faster it is moving away [52]. The expansion of space causes cosmological redshift to increase the wavelengths of light being received from the receding source. The amount of redshift indicates how distant they are. Cosmological redshift appears, effectively, like the relativistic Doppler effect, however, these concepts differ significantly. The Doppler effect is the result of an objects relative velocity through space as a wave is emitted and received. Cosmological redshift is caused by the expansion of space itself, and the passage of light through this ever-expanding area of space.

Hubble's law states that a galaxy's recession velocity v is proportional to its distance D from Earth [53]. This law can be expressed as

$$v = H_0 D$$

where H_0 is Hubble's constant (approximately 70 km/s/Mpc). The redshift z is expressed in terms of the emitted wavelength and observed wavelength as

$$z = \frac{\lambda_{emit} - \lambda_{obs}}{\lambda_{emit}}$$

For velocities much smaller than the speed of light c, the relationship between v and z is

$$z \approx \frac{v}{c}$$

In general, the relationship between between v and z is

$$1 + z = \sqrt{\frac{1 + v/c}{1 - v/c}}$$

For small distances, the relationship between the redshift and the distance of an object have a simple, linear relationship. For sources with greater redshift values, general relativity must be included when calculating the distance [54].

1.4.3 Distant Supernovae

In this research, the predictable and consistent nature of the type Ia supernova lends itself to preliminary calculations regarding the potential results of observing a distant, red-shifted supernova. The ELT and MICADO will be used to observe very distant objects in the infrared. The observed infrared light may have originally been emitted in the visible or ultraviolet range of the electromagnetic spectrum, before the effects of cosmological redshift made the light observable in the infrared. Astropy's cosmology package is used here, along with known magnitudes of type Ia supernovae in visible and UV bands to calculate the possible apparent magnitudes that may be observed in the infrared. Redshift values relate the observed and emitted wavelengths, as well as the apparent and absolute magnitudes.

Type Ia supernovae have peak absolute magnitudes close to -19 mag in the V band, -19 mag in the B band, -19.5 mag in the U band, and -18 mag in the uvw1 band, in the Vega magnitude system. These bands have central wavelengths of 544 nm, 437 nm, 346 nm and 260 nm respectively [55]. The J and K_s bands have central wavelengths of 1240 nm and 2160 nm respectively [56].

At a redshift of $z = 2.97$, the central wavelength of the V band is redshifted to the central wavelength of the K_s band. This redshift corresponds to a luminosity distance of $d = 25.6$ Gpc. This distance, and the absolute magnitude $M_B = -19$ mag can be used to find the apparent magnitude – which has been shifted to the K_s band – using the equation

$$m - M = 5 \log \frac{d}{10\text{pc}}$$

At this distance, the apparent magnitude of a type Ia supernova in the K_s band is predicted to be $m_{Ks} \approx 28$ mag. This approach can be used to find approximate apparent magnitudes of supernovae with other redshifts. A redshift value of 3.77 corresponds with the uvw1 band being redshifted to the J band, and a luminosity distance of $d = 34.1$ Gpc. The absolute magnitude of a type Ia supernova in the

uvw1 band is $M_{uvw1} = -18$ mag. The calculated apparent magnitude in the J band is $m_J \approx 29.7$ mag. At a redshift of $z = 1.84$, the distance of a source is $d = 14.3$ Gpc. This redshift value corresponds to the B band being redshifted to the J band. Using $M_B = -19$ mag, the calculated absolute magnitude is $m_J = 26.8$ mag. At a redshift of $z = 5.24$, the luminosity distance of a source is $d = 50.3$ Gpc; the U band is redshifted to the K_s band. The calculated apparent magnitude in the K_s band at this redshift is $m_{Ks} \approx 29$ mag. These hypothetical sources are very faint. Scopesim will be used to simulate the observation of point sources at magnitudes around this range.

1.5 Scopesim

Scopesim is a python package that is used to simulate astronomical observations with various instruments [57, 58]. This research consists of simulations of the MICADO camera and the ELT. Scopesim works with another python package called Scopesim Templates, which generates data describing a luminous celestial object. Scopesim performs operations according to parameters of the optical system, to transform source data as if it had passed through the optical system and recorded by the camera. The simulation yields a 2D image, and saves it as a FITS file. Changes can be made to the observation parameters, such as: the airmass, the right ascension and declination, photometric filters, and exposure time. Environmental conditions can also be modified, such as the target location, humidity, air pressure, atmospheric temperature and telescope temperature.

1.6 Scopesim Templates

Scopesim Templates is a python package that is used to generate source objects to use in Scopesim simulations. Each object contains spatial and spectral data about the source. The package offers options to generate stellar and extragalactic objects:

a single star, multiple stars, a star cluster, a star grid, a simple galaxy, a 3D galaxy, a spiral galaxy, or an elliptical galaxy. There are also templates for more general objects: a point source, a uniform source, a numpy array, or an image file. These objects require spectral properties to be specified; scopesim uses spectral data from the speXtra python library [59]. After generating any of these objects, the optical source is defined as the sum of one or more of the objects.

Scopesim Templates also offers calibration templates: an empty sky, a flat field, and a lamp with a specified emission line spectrum. The corresponding effects are automatically applied to the simulation, so they should be switched off if the calibration frames are used to reduce the data [60].

2 Simulating MICADO observations with Scopesim

Using Scopesim to gain insight into future use of the ELT was a multi-step process. When using scopesim, the python code has three main parts: the source parameters, the telescope parameters, and the observation. Here is a more detailed summary of what the code does:

- Load necessary packages and files
- Generate one or multiple objects with Scopesim Templates
- Set parameters of the observation
- Use the optical train to run a simulation
- Save the image as a FITS file

2.1 Input Objects

There are multiple functions in the Scopesim Templates package for generating source objects. In general, these functions require coordinates, magnitudes, and spectral types to be specified; these parameters will vary. After generating and defining a source, the source can be viewed without passing it through an optical system. Here are some examples of sources, before the observation, in Figure 9. These plots are helpful when troubleshooting code by determining if the intended source was successfully generated. These example sources will be shown later in this section, with an observation being simulated.

Each source generated with scopesim templates, except for an empty sky, includes a source spectrum. The spectrum of a source can be specified in the function if the source is a star, a point source, a galaxy, an array, or a fits file. Some source types have spectral properties already established, such as a star cluster. If a source contains multiple objects with different spectra, scopesim will produce a spectrum

for each source type. Scopesim gets its spectra from the speXtra database. Figure 10 shows two examples of spectra from Scopesim source objects.

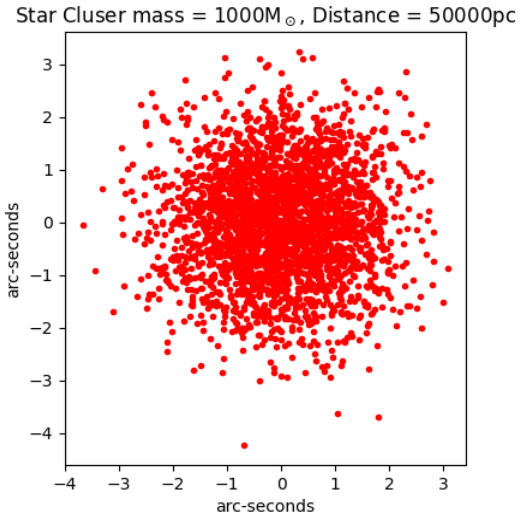

(a) A star cluster with 1000 solar masses, a half light radius of 0.3 parsecs, and a distance of 50 kpc.

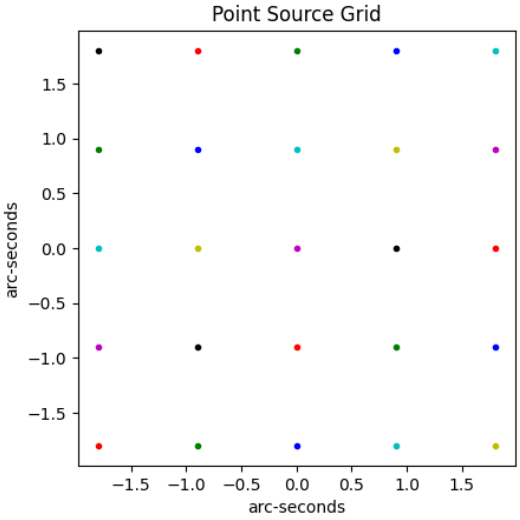

(b) A set of point sources, positioned in a 5×5 grid. The distance between points is 0.9 arc-seconds.

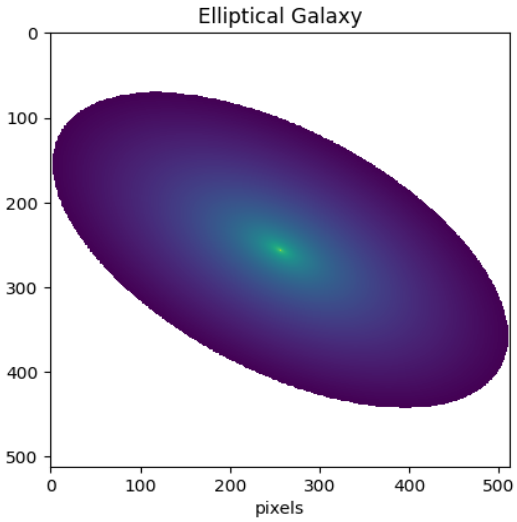

(c) An elliptical galaxy with a half-light radius of 3 arcsec, and a magnitude of 14.

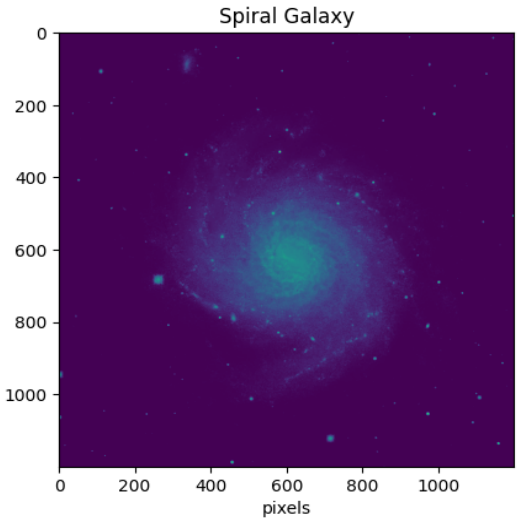

(d) Spiral galaxy NGC1232.

Figure 9: Source objects, not observed.

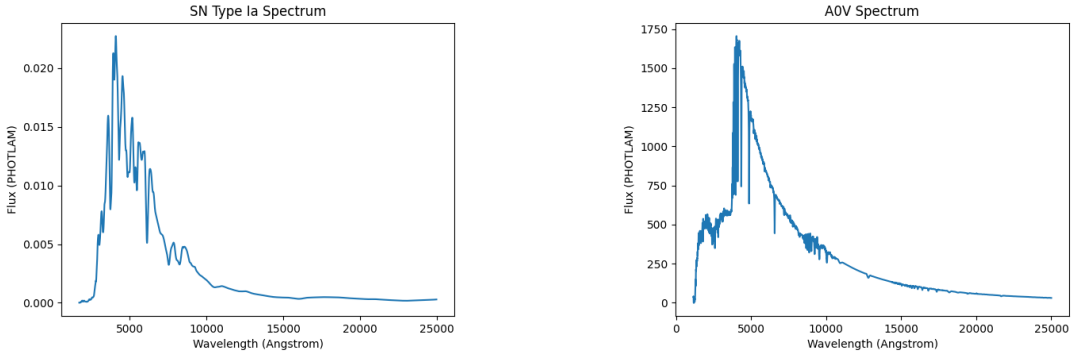

(a) Type Ia Supernova

(b) Type A0V Star

Figure 10: Example spectra from Scopesim source objects

2.1.1 Observing with MICADO and the ELT

The following sections will display examples of different objects generated with scopesim templates, and observed with the scopesim optical train function. The units in each image are photons per pixel. The default parameters of these observations are displayed in table I.

Default Parameters		
AO System SCAO	Pixel Scale 4 mas	Size 1024×1024
Exposure Time 1000 s	Filter K_s	Airmass 1.2
Temp 7°C	Humidity 0.1	Air Pressure 0.755 atm

Table I

The MICADO detector has a size of 12288×12288 pixels. The field of view, when the pixels are 4 mas wide, is 50.5"×50.5". This impressive spatial resolution will be useful in many scientific endeavors. However, the focus of this research is

very distant point sources, where such a large image size is not needed. Figure 11a shows a simulated observation of a star cluster that contains 100000 solar masses, at a distance of 50 kpc, using the entire field of view. These stars serve as examples of point sources with varying magnitudes. It would be easier to visually assess the PSF of MICADO using a more narrow field of view. For this reason, the figures presented in this section after Figure 11a will have a size of 1024×1024.

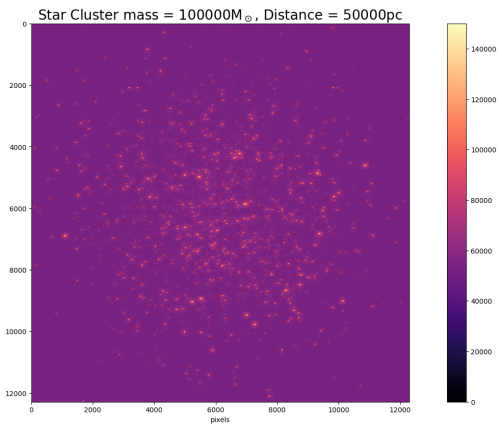

(a) A star cluster simulation, in the K_s band, with a pixel scale of 4 mas, and a field of view of 50.5"×50.5".

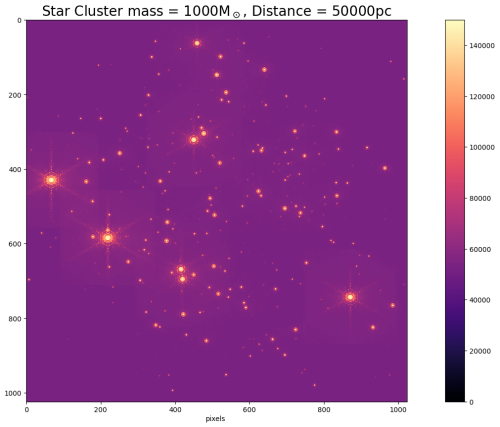

(b) A star cluster simulated with a 4mas pixel scale, and a field of view of 4.1 arcseconds.

Figure 11

2.1.2 Star Clusters

A simple way to simulate many stars together is to generate a star cluster. Rather than specifying locations, magnitudes, and spectral types of many individual stars, the star cluster function receives the total mass and radius of the cluster, its distance and location. The output is a random star cluster with the specified properties. Studying distant stellar populations is one of the intended uses of MICADO, therefore the star cluster function is an important, relevant feature of scopesim. Figure 11b is an observation of the same random star cluster shown in Figure 9a. This

simulation image, as well as the others that follow in this section do not show the full field of view of the MICADO, because the PSFs in the images would be difficult to see, and the full field of view does not benefit this examination of the image quality. The size of the following images is 1024×1024. With a 4 mas pixel scale, this size yields a field of view of 4.1 arcseconds. With a 1.5 mas pixel scale, the field of view is 1.54 arcseconds. Figure 11b can be compared to Figure 11a, which shows another star cluster equally distant from the ELT.

2.1.3 Stars

To simulate multiple stars with more specific parameters, the stars function can be used. This function takes a photometric filter name for scaling the stars, a list of magnitudes, a list of spectral types, and lists of x and y coordinates.

2.1.4 Galaxies

Scopesim has multiple functions for producing galaxies. The spiral galaxy function called "spiral two component" makes a galaxy based on data from galaxy NGC1232. This function has arguments that ostensibly allow the angular size and the magnitude of the galaxy to be varied. However, only the size parameter appears to work correctly; all changes to the magnitude leave the image unchanged. Figure 12a shows an example of the spiral galaxy observation. The galaxy NGC1232 is located at a distance of approximately 15 Mpc [61].

The elliptical galaxy function makes a generic elliptical galaxy, with parameters for its size, ellipticity, brightness, Sersic index, and spectrum. Figure 12b shows an elliptical galaxy with a magnitude of 14. It's important to note that while adjusting the radius of this galaxy does change the distribution of light, there appears to be an outer perimeter, beyond which, scopesim does not add any light from the galaxy. This outer limit can be seen clearly in Figure 12b.

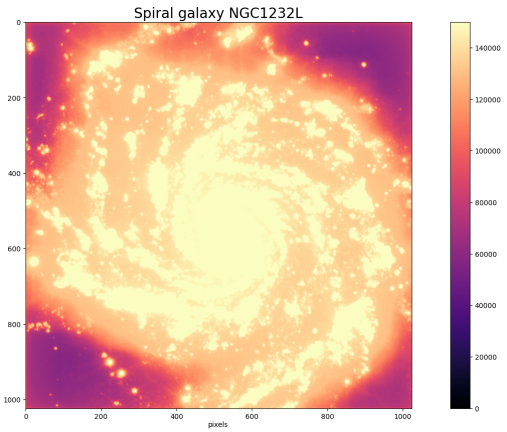

(a) Spiral galaxy NGC1232, with an exposure time of 1000s.

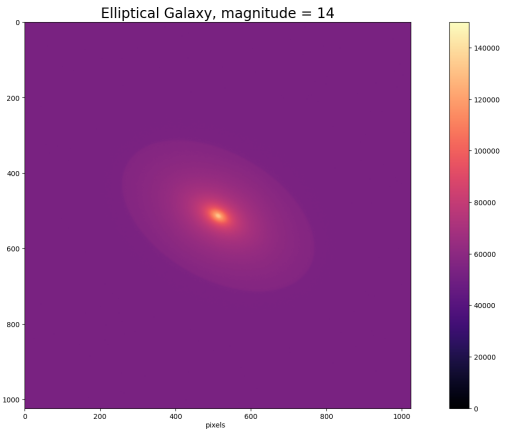

(b) An elliptical galaxy with a magnitude of 14, a radius of 2 arcseconds, and an exposure time of 1000 seconds.

Figure 12

The scopesim templates documentation lists two other galaxy functions: galaxy and galaxy3d. These functions take similar arguments to the other functions offered. At the time of this research, these functions do not yield an observable source object.

2.1.5 Point Sources

Point sources have been the most utilized object type in this research. Point sources can represent any object with a sufficiently small angular size, and a spectral type in the speXtra library. The point source function is used in this research primarily to simulate supernovae observations. The function takes a spectrum, magnitude, photometric filter, and coordinates. Simulating point sources is an easy way to view the point spread function of the simulated optical system. Figure 13 shows a set of point sources with varying magnitudes in the K_s band. This grid is useful for determining how visible point sources of various magnitudes will be with the utilized observation settings.

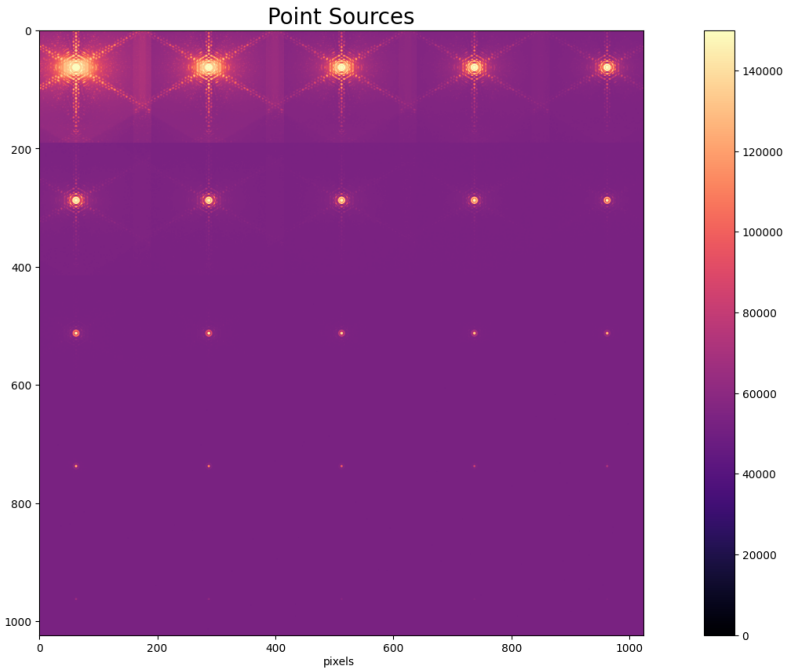

Figure 13: A grid of 25 point sources with magnitudes ranging from 15 to 27 mag in the K_s filter band.

2.1.6 Source From File

Scopesim templates also offers functions called "source from file" and "source from array" which are supposed to take a 2D array, either from a fits file, or a numpy array respectively, and generate a light source to be observed with scopesim. These functions, however, do not yield an observable source. These functions should be available to use at a later time, as scopesim is still being developed.

2.2 Carrying Out Observations

This section shows examples of sources being observed with MICADO to compare different optical parameters.

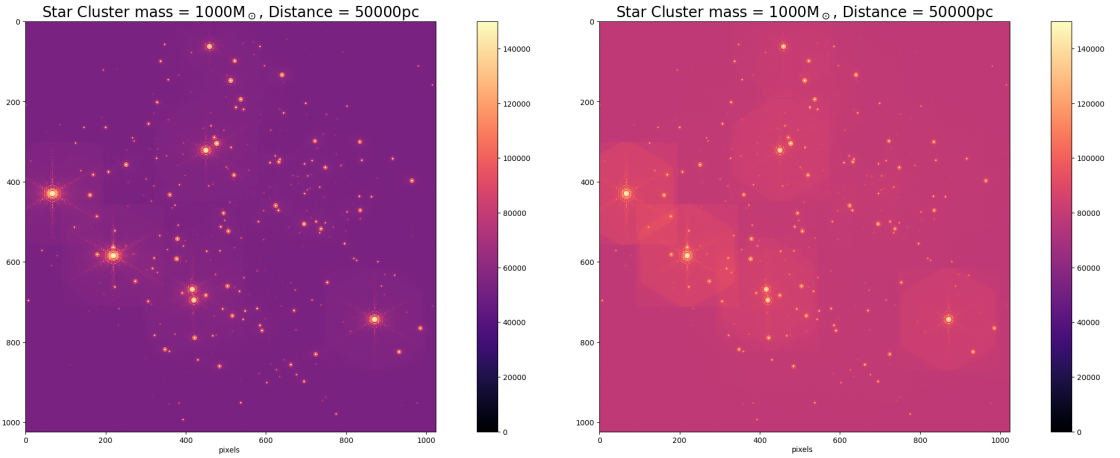

(a) A star cluster simulated with SCAO.

(b) The same star cluster, simulated with the same parameters, except that MCAO is used.

Figure 14

2.2.1 SCAO vs MCAO

MICADO has two AO systems: MCAO and SCAO. Scopesim supports simulations that use either of these systems. Each AO system is simulated with a static PSF distribution. The examples shown thus far have simulated observations with SCAO. To compare the quality of observations between these systems, the star cluster shown previously is also simulated using MCAO, shown in Figure 14.

The observation with MCAO has more prominent background radiation, and a wider distribution of the point spread function. So far, it appears that SCAO is more effective at providing a sharp image. The MCAO simulation also appears to limit the radius of a PSF, beyond which the brightness abruptly cuts off.

2.2.2 The Pixel Scale and Field of View

The pixel scale of the MICADO camera can be either 4 mas pixels (a 50.5" x 50.5" field of view), or 1.5 mas pixels (an 18" x 18" field of view). Both of these options are supported by scopesim. The examples shown so far have had a pixel scale of 4 mas. Figures 15a and 15b are shown side-by-side to compare the quality of images

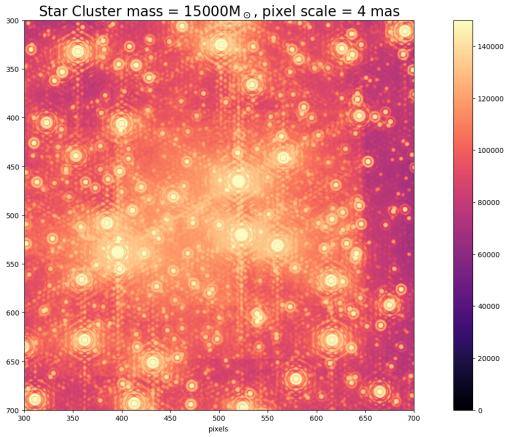

(a) The previously shown star cluster simulation with a 4 mas pixel scale, and SCAO system, cropped to compare the simulation to a more narrow field of view.

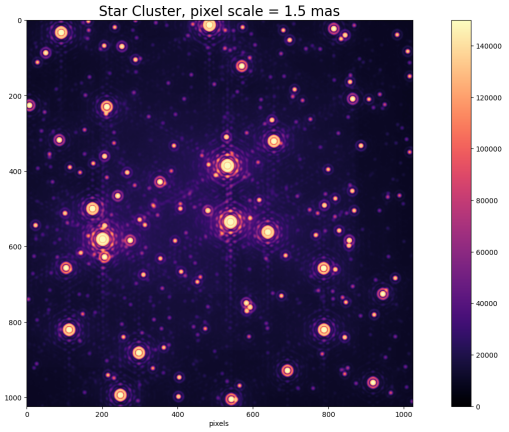

(b) The same star cluster simulated with a 1.5 mas pixel scale.

Figure 15

with these pixel scales. Figure 15a is from a simulation of the 4 mas pixel scale. It has been cropped further to show the middle of the image, at a field of view that is nearly the same as the one shown for the 1.5 mas pixel scale. These figures show the same set of stars, with other parameters remaining unchanged between them. A star cluster with a greater density has been used in these figures to show the usefulness of the 1.5 mas pixel scale when viewing an area that is densely populated with light sources.

The larger pixel scale has more background radiation per pixel, and the stars appear brighter. The width of the point spread function appears the same or similar in each image. More exposure time is needed for an equivalent observation in the 1.5mas pixel scale, relative to the 4mas pixel scale.

2.2.3 Environmental Parameters and Telescope Pointing

The optical train has a large set of parameters that can be modified to customize a simulation. Some notable changes that can be made represent environmental conditions that can vary, and potentially impact the outcome of an observation, namely, atmospheric temperature, humidity, and air pressure. This section also considers changes in airmass.

To investigate the impact of environmental conditions and airmass on an observation, the star cluster in Figure 11b, is shown again in Figure 16a, alongside observations of the same star cluster with varying conditions. In four observations, all but one parameter are unchanged, so that each change can be assessed individually. It is also important to consider how multiple environmental changes can potentially intensify any changes, due to the complex nature of the atmospheric system. The final simulation combines all of the previous environmental changes. The values used in these simulations are intended to be unlikely and **extreme**, so that if a simulation doesn't appear significantly different from the default simulation, it is evident that scopesim does not calculate a drastic change in the outcome of observing with any possible value of the varied parameter.

The changes to the environment and telescope pointing have changed the level of background radiation present to varying degrees. The point spread function appears not to be significantly changed. The most drastic change appears when the temperature is changed from 7°C to 20°C; the amount of background radiation increases with the increase in temperature. The simulation with the humidity set to 1, the highest relative humidity possible, does not visibly appear to be different from the simulation with default parameters. The simulation with an air pressure of 1 atm, a pressure unlikely to occur at the location of the ELT, also appears to be negligibly different from the simulation of default parameters. The simulation with an airmass of 2.25 has slightly more background radiation than what appears in the

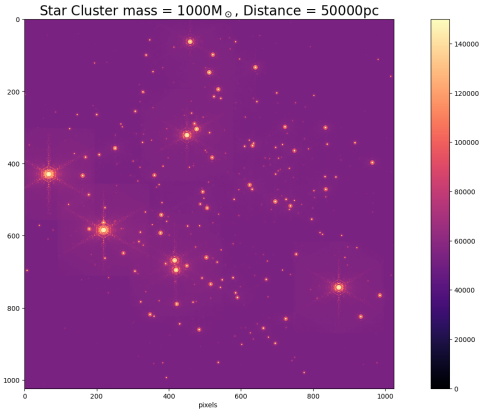

(a) The star cluster observed with default parameters.

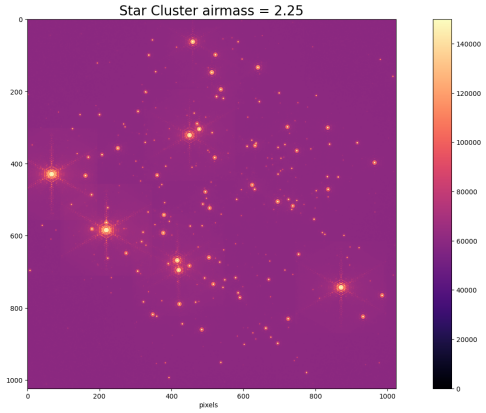

(b) The star cluster observed an airmass of 2.25 instead of the default airmass value of 1.2.

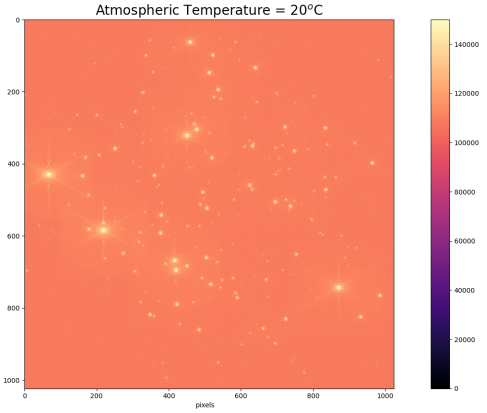

(c) The star cluster observed with an atmospheric temperature of 20°C instead of the default value of 7°C.

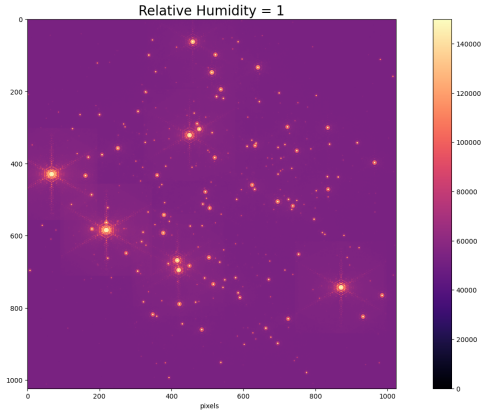

(d) The star cluster observed with humidity of 1 instead of the default value of 0.1

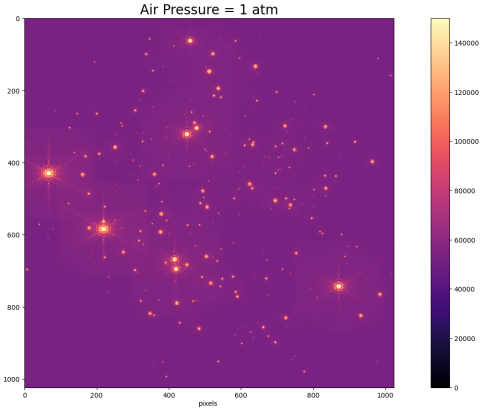

(e) The star cluster observed with air pressure of 1 atm instead of the default value of 0.755 atm.

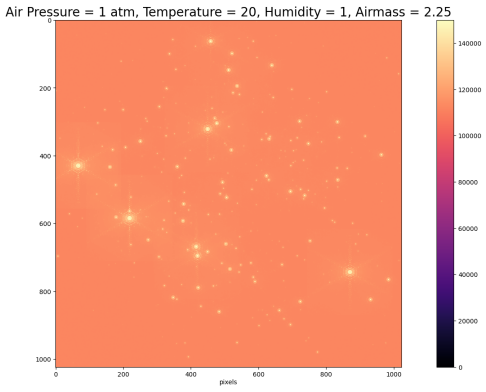

(f) The star cluster observed with an airmass of 2.25, an atmospheric temperature of 20°C, humidity of 1, and air pressure of 1 atm.

Figure 16

simulation of default parameters. This is not the expected outcome of drastically increasing the airmass. An increase in airmass should cause a loss in brightness of the image, as well as a widening of the PSF [62].

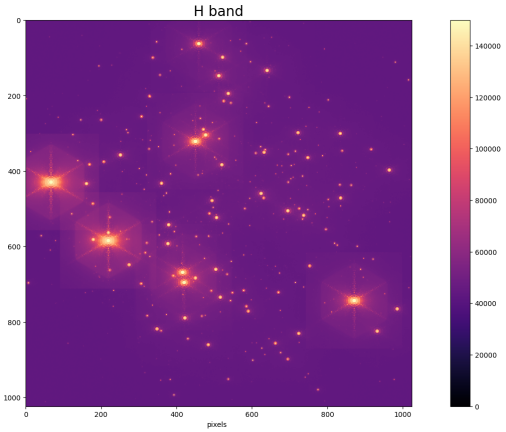

(a) The star cluster observed with the H filter.

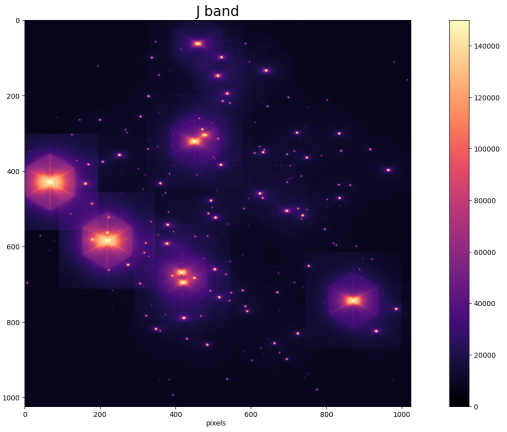

(b) The star cluster observed with the J filter.

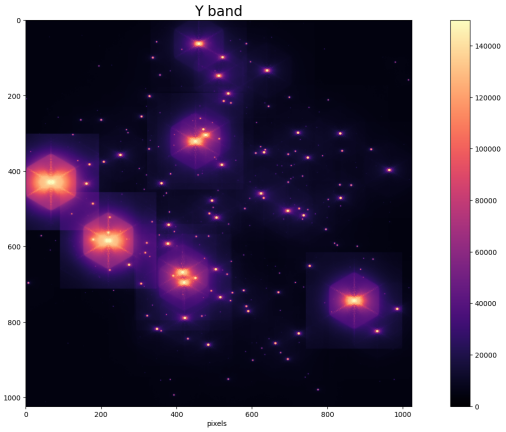

(c) The star cluster observed with the Y filter.

Figure 17: A star cluster observed in the H, J and Y bands.

2.2.4 Photometric Filters

Scopesim offers an assortment of photometric filters, split between two MICADO filter wheels. Light of different wavelengths will interact with the environment and

optical system differently, and thus will yield different point spread functions. The same star cluster used to compare other scopesim features is observed in the J, H and Y, bands (Figure 17 below). The complete list of filters supported by scopesim is in the MICADO YAML file.

These figures all appear very visually different. The cluster in the H band has considerably more background radiation than what is seen in the other images. A wide, faint hexagonal area of light appears around the brighter stars. The cluster observed in J and Y bands feature this pattern more prominently, with larger areas of high intensity light.

2.3 Empty Sky Calibration

Scopesim has a set of calibration functions. A very useful function in this research is the empty sky function, which simulates an observation containing only background radiation. Figure 18c shows an empty sky that has been observed with the K_s filter, and an exposure time of 1000 seconds.

To reduce the presence of background radiation in an observation of an object, an empty sky should be simulated with the same parameters as the object observation, so that the background radiation in each is equivalent. The empty sky file can be used to subtract the radiation from object observation. The star cluster simulation in Figure 11b appears to have a significant amount of background radiation diminishing the view of the stars. Here it is shown alongside the reduced image, in Figures 18a and 18b. The reduction of background radiation facilitates the observation of the point spread function displayed by each star, and increases the visibility of dim objects.

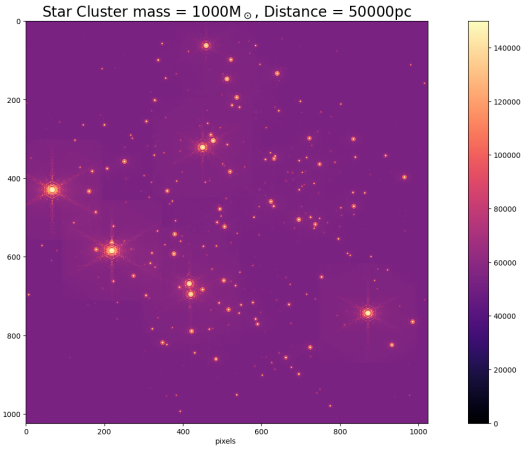

(a) The star cluster observed with the K_s filter.

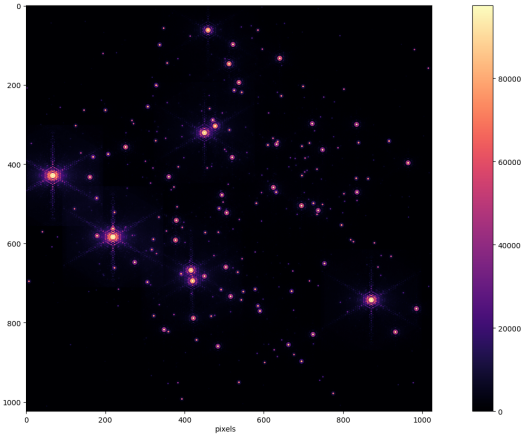

(b) The same star cluster with background radiation subtracted from the image.

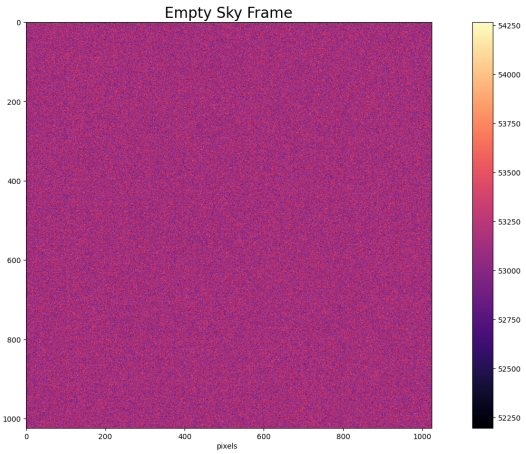

(c) An empty sky observed in the K_s band.

Figure 18: A star cluster observation, with and without the subtraction of an empty sky frame, and the empty sky frame.

3 Metrics For Analyzing the PSF

The following section introduces 3 methods for quantifying the area of a point spread function produced by scopesim, by determining the FWHM of the cross-section of the PSF, the Strehl ratio, and the signal-to-noise (SNR) of the PSF.

3.1 Intensity Cross-Section of a Point Source Image

For each point source image that is analyzed, a 1-dimensional set of pixels is selected from the image, such that the center of the pixel set is the center of the point source. The values in the pixel set are then plotted, showing light intensity vs position. The FWHM of each PSF is obtained from each of these sets. As with the images shown in the previous section, the intensity units are in photons per pixel.

To obtain an accurate value for the FWHM, the selected pixels must span an area of space that is wider than the PSF, and contain pixels that are only illuminated by background radiation. The difference between the background intensity and the maximum light intensity is used to find the half maximum. The full width is the greatest distance between two pixels with values greater than or equal to the half maximum. The PSFs generated by scopesim do not strictly decrease in intensity with increased distance from the center of the point. There are zigzags in the PSFs. Therefore, the PSFs may have areas with intensity less than the half maximum, within the span of the FWHM. The simulations evaluated with this method have been reduced using a blank sky image, simulated with identical observation parameters.

The PSFs generated by scopesim do not have circular symmetry. The images of point sources display a hexagonal pattern. Therefore, the distribution of a PSF obtained from a 1-dimensional slice of an image is dependent on the axis through which a set of points is selected. At least two slices should be considered for a comprehensive analysis. Horizontal and vertical segments are the most convenient

satisfactory choices. Figure 19 shows a point source with a magnitude of 18, viewed with SCAO in the K_s band. The background radiation has been subtracted. Adjacent to this plot are the two PSF cross sections. The horizontal cross section has a FWHM of 13 pixels, and a vertical cross section FWHM of 23 pixels. Figure 20 shows an Airy disk distribution with the same magnitude, alongside its vertical and horizontal cross sections. The FWHM value of the Airy disk cross-section is 3 pixels.

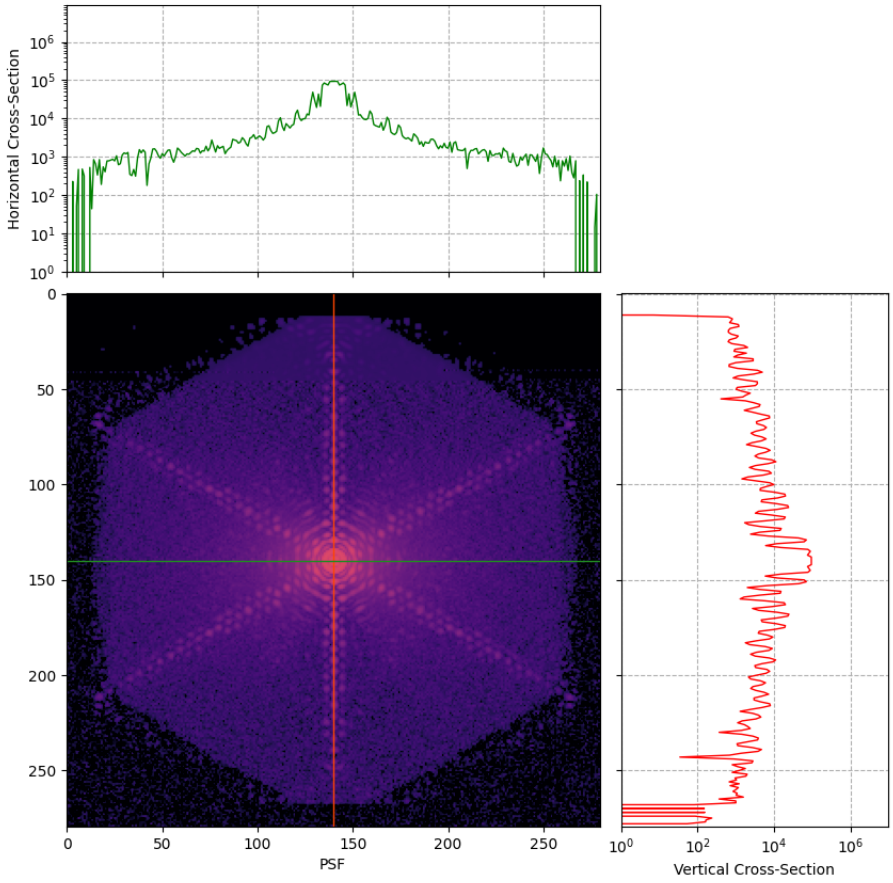

Figure 19: A point source with a magnitude of 18 mag in the K_s band, and the cross section of the PSF through the horizontal and vertical axes. The lines on the image indicate where data was taken to plot and analyze the PSF. The brightness of the center of the PSF is cut due to effects of saturation of the detector.

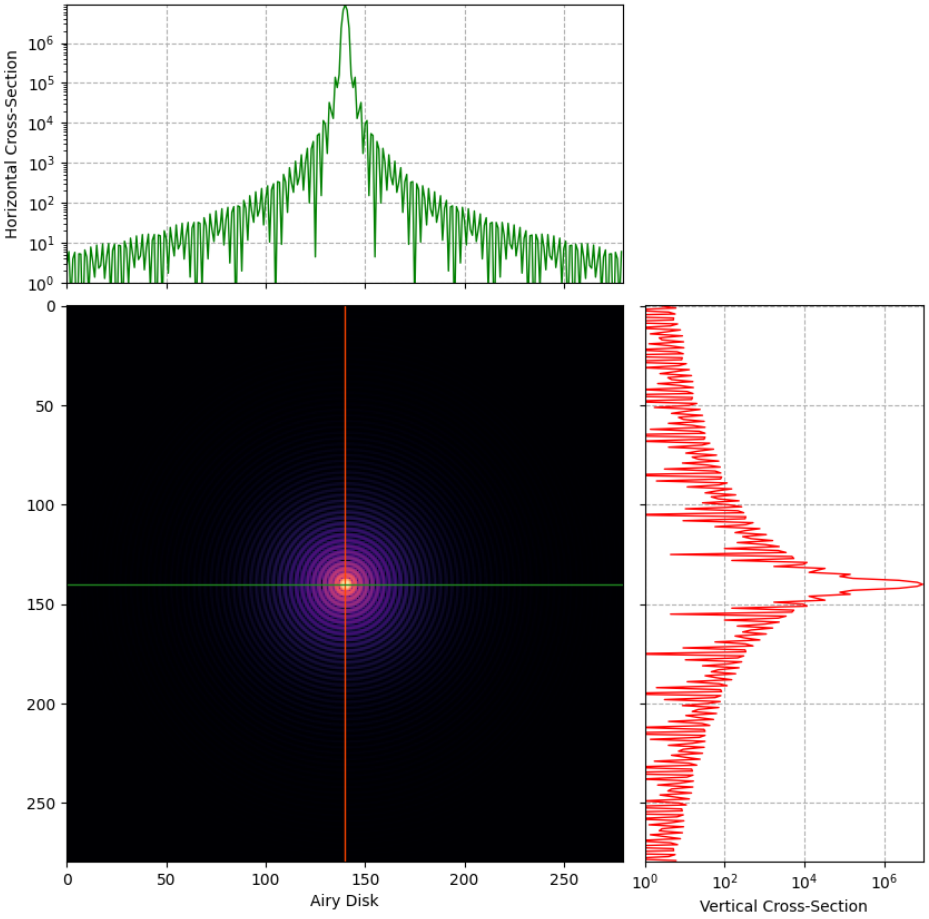

Figure 20: An Airy disk distribution, with the same magnitude as the PSF shown in Figure 19, (18 mag), and its cross section plots through the horizontal and vertical axes.

3.2 The Strehl Ratio

The quality of a PSF can also be quantified with the Strehl ratio. Each AO system and pixel scale are compared using the Strehl ratios that are calculated for each observation parameter. The effect of airmass on the PSF is assessed in the same manner.

To calculate the Strehl ratio, the Airy disk distribution was calculated for each band central wavelength and each pixel scale. For each simulated PSF, the corresponding Airy disk distribution was normalized to the total flux of the PSF. The Strehl ratio was then found by simply taking the ratio of the peak of the PSF and the peak of the Airy disk. For a visual example, consider, figures 19 and 20, which show a PSF and Airy disk, respectively. The total flux in the images is equal. The strehl ratio is the ratio of the peak intensities in each image.

Scopesim simulates the detector as having a saturation limit. This will necessarily cause the Strehl ratio to be unreasonably low for any exposure that is long enough to allow the central light intensity to reach that limit. It is important to verify that the detector is not over-saturated, to obtain a valid Strehl ratio.

Figure 21 shows the Strehl ratios of point source images generated with each AO system and pixel scale, in the K_s, J and Y bands. The magnitude and exposure time for each PSF are 22 mag and 1000s respectively. For each band, the highest Strehl ratios are found when SCAO is used for an observation. The MCAO system corrects for atmospheric turbulence over a wider area than SCAO, while SCAO makes a more effective correction over a smaller area. Thus, when observing single point sources, without a need to consider the surrounding area, SCAO will yield more favorable results. The 1.5 mas pixel scale, used with SCAO, produced the highest Strehl ratios. In the K_s, J and Y bands, the Strehl ratios obtained with these parameters are 0.54, 0.20, and 0.13 respectively. Scopesim does not offer the option to generate a MICADO PSF without an AO-correction.

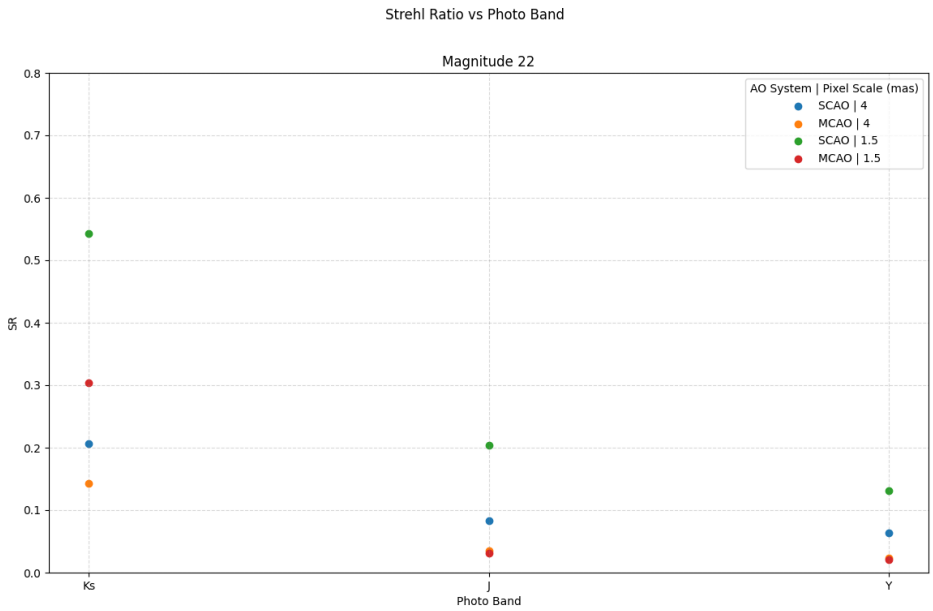

Figure 21: Strehl Ratio of a PSF with magnitude 22, using SCAO, MCAO, a 4 mas pixel scale, and 1.5 mas pixel scale, and the K_s, J, and Y bands.

The highest Strehl ratios were observed in the K_s band. This can be explained by considering the relation between the Airy Disk width, and the observed wavelength. The width of the Airy disk is proportional to the wavelength. For a longer wavelength, such as 2.16μm in the K_s band, the Airy disk will be wider than an Airy disk with a wavelength of 1.24μm or 1.03μm, in the J or Y bands, respectively. With a wider Airy disk, the central height of the distribution is lower, relative to the total flux. Taking the ratio of the PSF peak to this lower Airy disk peak will yield a higher Strehl ratio.

3.2.1 Airmass

The airmass of an observation can have a significant impact on the quality of the PSF [62, 63]. To further assess the effects of airmass, as purported by Scopesim's simulation results, the SCAO system and 1.5 mas pixel scale were selected for simulating point source observations in the K_s, J and Y bands, with varying airmass

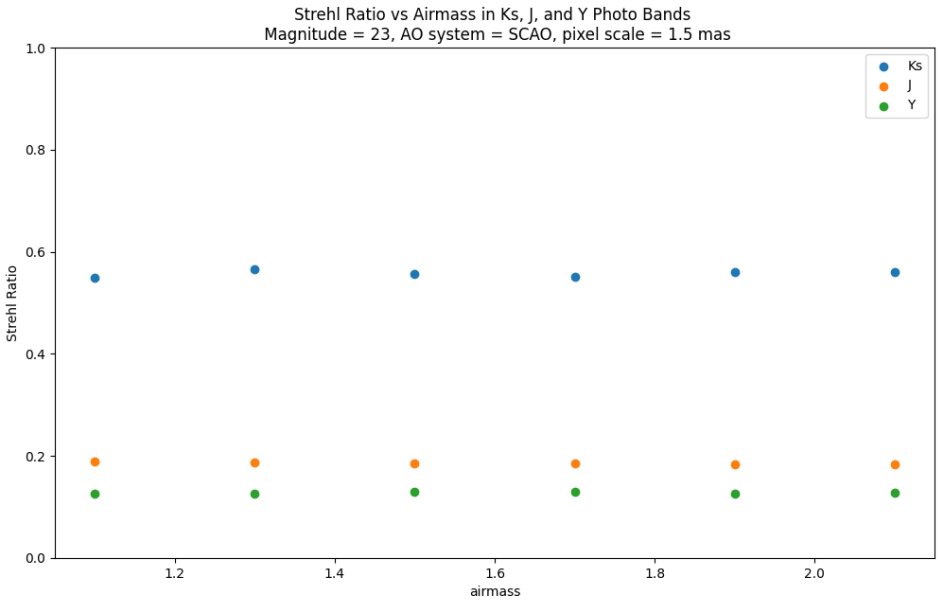

Figure 22: Strehl Ratio vs Airmass in the K_s, J, and Y bands.

values. The results are shown in Figure 22. The point source has a magnitude of 23 in all observations. Each observation has an exposure time of 1000s. The average Strehl ratio in the K_s band is 0.56; the range of the Strehl ratios in this set is less than 0.02. The average Strehl ratio in the J band is 0.19; the range of the Strehl ratios in the J band is within 0.006. The average Strehl ratio in the Y band is 0.13; the range of the Strehl ratios in the Y band is 0.004. The calculated Strehl ratios for varying airmass values have very little variation in each of the tested bands.

Airmass is an important consideration when planning an astronomical observation. However, varying the airmass value in scopesim simulations does not yield any change in the Strehl ratio of a PSF. In reality, one would expect an increase in the airmass to widen a PSF, and yield a lower Strehl ratio [62].

3.3 Signal-To-Noise Ratio

The signal-to-noise ratio is the ratio of the intensity of the point source (the signal) to the uncertainty of the intensity (the noise). It is calculated by selecting an aperture around a point source and finding the average signal value inside the aperture, then selecting an area near the point source and calculating the standard deviation of the noise in that area. The ratio of these values is the signal-to-noise ratio [64–66]. Figure 23 shows the signal-to-noise ratio of a set of point source observations with magnitudes ranging from 22 to 29 in the K_s band, observed using SCAO and the 4 mas pixel scale. An aperture radius of 4 pixels was used. The point source with a magnitude of 26 has a signal-to-noise ratio of 4.5. The points that are dimmer than this are barely detectable or undetectable.

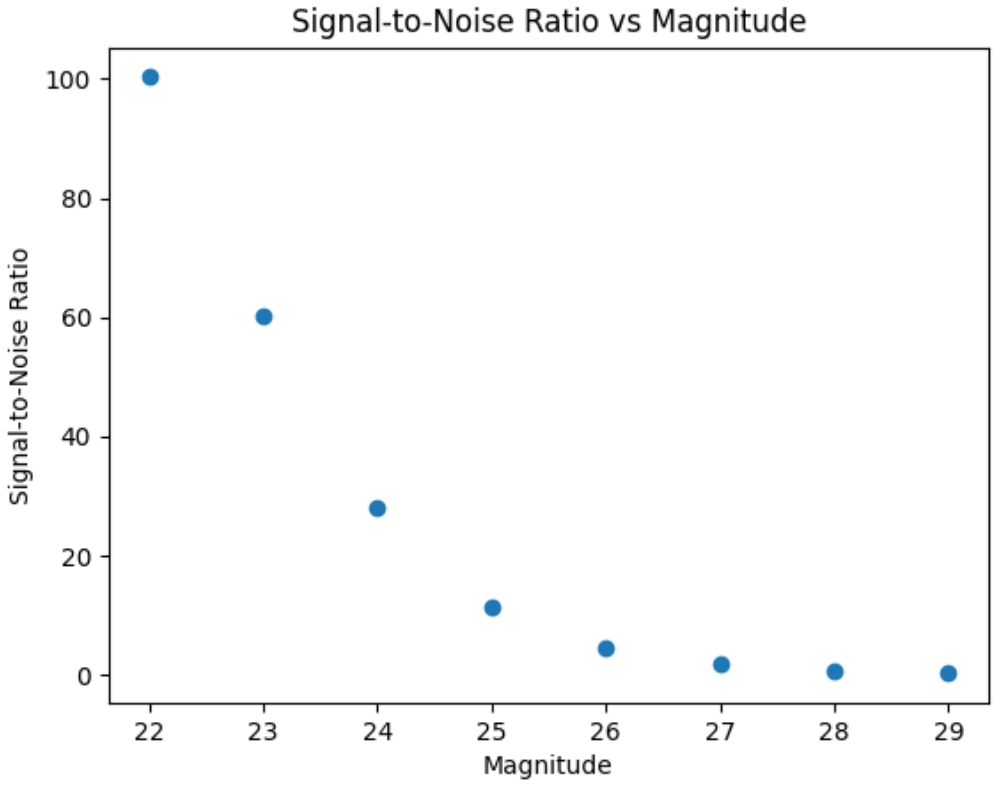

Figure 23: Signal-to-noise ratio vs magnitude, in the K_s band, with an exposure time of 1000 s.

4 Observing a Supernova and a Galaxy

The analysis tools introduced in the previous section were used to analyze simulations of a supernova observation. The following steps were taken to make the simulations more realistic:

- Each point source was simulated with a host galaxy.
- Multiple exposures were simulated, with the telescope position changed for each exposure.
- The detector exposure time was set to 1s.
- The total integration time of each observation was 1h.
- Apparent magnitudes and angular separations between the host galaxy and supernova were based on calculations similar to those in section 1.4.3, and other calculations made using astropy's cosmology package.

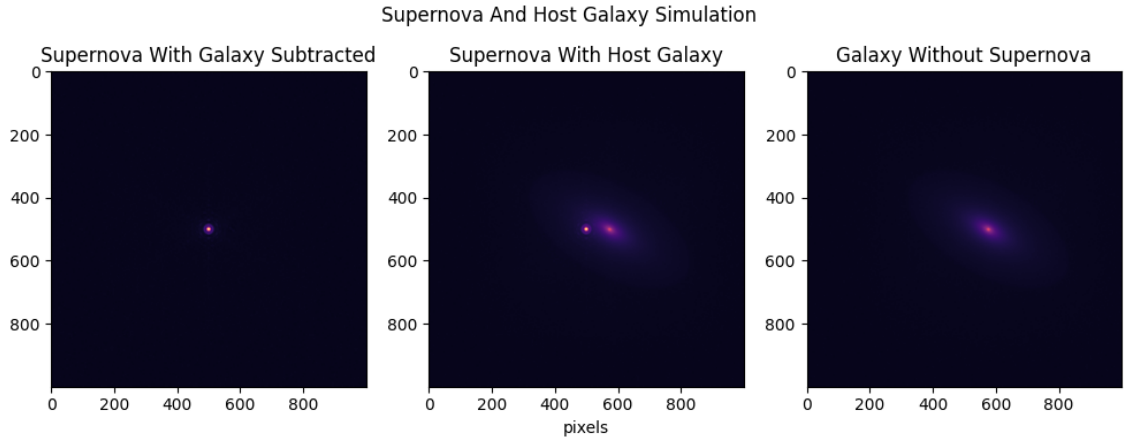

Figure 24: Difference imaging example: host galaxy with and without a SN; SN with the galaxy flux subtracted. Supernova magnitude: 21 mag, filter: K_s, exposure time: 1000 s, galaxy offset: 0.11 arcsec.

An empty sky frame was subtracted from each exposure. Observations of each host galaxy were simulated without a supernova, so that the flux from the host galaxy

could be subtracted from each frame. Figure 24 shows an example of a host galaxy that has been simulated with and without a supernova, and the flux from the host galaxy subtracted from the supernova-galaxy system.

This image-subtraction method is intended to simulate the use of difference imaging in astronomy. Difference imaging can be used to improve photometric analysis and enable detection of faint transients against a host galaxy [67–69]. The simulated difference images do not account for some of the challenges of using difference imaging, such as: changes in airmass, detector noise, and atmospheric conditions. Such complications would require a pre-supernova image to be modified using more advanced algorithms than what is within the scope of this project.

Only the SCAO system is simulated in this section, for a few reasons. In the previous section, where the Strehl ratio is introduced, Figure 21 shows that the use of SCAO produces PSFs with higher Strehl ratios than when MCAO is used. This is consistent with what is expected from these AO systems. SCAO is expected to give a superior AO correction over a narrow field of view, compared to MCAO providing a moderate AO correction over a larger field of view [70]. For analysis of a single point source close to a reference source, SCAO is the optimal choice. For imaging across a wider area, MCAO should be used. The analyses in this section are of a single point source in each simulation; SCAO would likely be used in observations of this type. The background flux in an image is significantly higher when MCAO is simulated. This is likely an error in scopesim. The amount of background radiation in an image should be unchanged by the AO system used [71]. Thus, analysis of simulations that use MCAO should be done later in the development in Scopesim.

Observations were simulated using the K_s, J and Y bands, the 4 mas and 1.5 mas pixel scales, default atmospheric parameters, and default airmass, shown in table I, and a 1 hour exposure time. For each filter band and pixel scale, 3 sets of observations were made: with the projected distance between the supernova and the

center of the host galaxy set to 500 pc, 1 kpc, and 2 kpc. Each set of observations uses the same galaxy-supernova system, with varying distances of the system from the telescope. The signal-to-noise ratio, Strehl ratio, and FWHM values were derived for each observation. The signal-to-noise ratios were plotted as a function of redshift. The magnitudes of the supernovae were set to represent Type Ia supernovae at peak luminosity.

4.1 Angular Resolution

When simulating supernova-galaxy systems at very large distances, it's important to consider whether or not the optical system will be able to resolve the center of the galaxy and the supernova as two discrete points. Figure 25 was created using FlatLambdaCDM (Flat Lambda Cold Dark Matter), from astropy's cosmology package, with the Hubble constant $H_0 = 69.6$ km/s/Mpc and matter density parameter $\Omega_m = 0.286$; the plot shows the angular scale of an area in space vs the redshift of the object being viewed. With this model, the largest angular scale is 8.6 pc/mas, occurring at a redshift of 1.5.

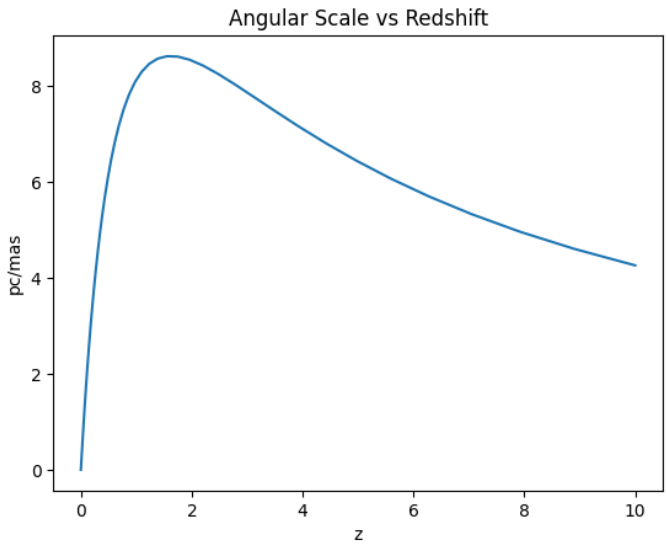

Figure 25: The angular scale of an area in the sky (pc/mas) vs redshift.

The limiting case of the systems shown in this section is the supernova with a projected distance of 500 pc from its host galaxy, at a redshift of 1.5. For an observation using the 4 mas pixel scale, the displacement between the supernova and the center of the galaxy is:

$$500 \text{ pc} \times \frac{\text{mas}}{8.6 \text{ pc}} \times \frac{\text{pixels}}{4 \text{ mas}} = 15 \text{ pixels} \tag{2}$$

When the 1.5 mas pixel scale is used, the number of pixels is 39. For each of these pixel scales, if the calculated FWHM of a PSF is greater than the number of pixels needed for the limiting case, it will be important to check if the system can be resolved.

4.2 Observation Results

Figure 26 shows the SNR vs redshift of each observation in the K_s, J and Y bands. Each projected distance is plotted separately, with the two pixel scales plotted together. For each set of observations, the 4 mas pixel scale yields higher SNR values at every redshift. SNR values vary slightly for each projected distance. In the K_s band, the SNR values are very low for redshifts greater than 1.5. To observe this type of supernova at a greater redshift, longer exposure times are needed. In the J band, the supernova cannot be observed at redshifts greater than 3. In the Y band, the supernova cannot be observed at redshifts greater than 2. The SNR values are the lowest for observations in the K_s band, and highest for observations in the Y band. The detector has greater sensitivity at shorter wavelengths.

Pixel Scale	Measurement	K_s	J	Y
1.5 mas	FWHM (pixels)	9	4	4
	Strehl ratio	0.55±0.02	0.22±0.02	0.16±0.005
4 mas	FWHM (pixels)	3	1	1
	Strehl ratio	0.56±0.04	0.26±0.02	0.18±0.01

Table II: FWHM values and Strehl ratio values of supernovae in the K_s, J and Y bands.

Table II shows the FWHM and Strehl ratio values of each supernova observed in the K_s, J and Y bands. In the K_s band, only the two lowest redshift values yielded results that could be used to calculate valid values for the FWHM and Strehl ratio

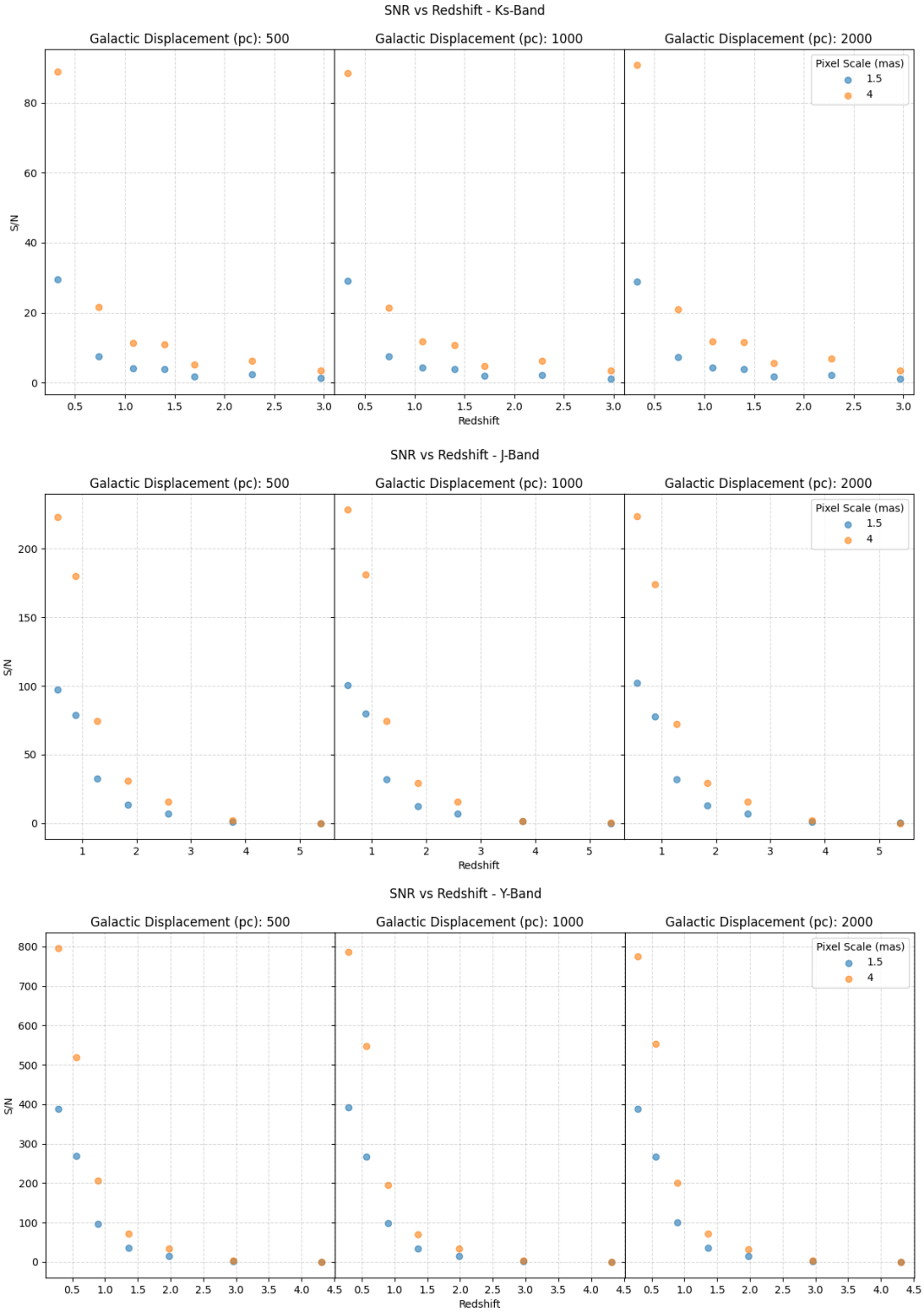

Figure 26: SNR vs redshift for projected distances of 500pc, 1kpc and 2kpc between the center of the host galaxy and the supernova, in the K_s, J and Y bands.

when the 1.5 mas pixel scale was used. When the 4 mas pixel scale was used, all but the highest redshift value yielded results that could be used to obtain valid values. When using the 1.5 mas pixel scale, the FWHM of a PSF is 9 pixels; when using the 4 mas pixel scale, the FWHM of a PSF is 3 pixels. These values are equivalent to 13.5 mas and 12 mas respectively.

In the J band, when the 1.5 mas pixel scale was used, the four lowest redshift values yielded results that could be used to calculate the FWHM and Strehl ratio. Using the 4 mas pixel scale allowed supernovae with the five lowest redshifts to be observed, and used to calculate FWHM and Strehl ratio values. When using the 1.5 mas pixel scale, the FWHM of a PSF is 4 pixels; when using the 4 mas pixel scale, the FWHM of a PSF is 1 pixel. These values are equivalent to 6 mas and 4 mas respectively.

Observations in the Y band have the lowest Strehl ratio values. The FWHM values for each pixel scale are the same as those found for observations in the J band. For each pixel scale, only the five lowest redshift values yielded results that could be used to calculate FWHM and Strehl ratio values.

For each band and pixel scale, the FWHM values are constant across the set of redshift values and projected distances. The SNR and Strehl ratio values changed very little with the change in position of the supernova. Having a small, but non-zero change in these values demonstrates that in Scopesim simulations, the flux distribution obtained from observing a point source and galaxy together does not equal the sum of the fluxes of each source observed separately. Therefore, there is value in simulating the observation of a constant celestial object, both with and without a transient light source, and subtracting the flux from the constant object from the frame that contains the transient object.

In the K_s band, supernovae with redshifts higher than 2 could not be detected. In the J and Y bands, supernovae with redshifts higher than 3 could not be detected.

In the J and Y bands, the Strehl ratio values appear slightly higher when the 4 mas pixel scale is used. In each band studied, the FWHM values in mas appear slightly lower when the 4 mas pixel scale is used.

The SNR values and detection limits are a result of the exposure time used. The SNR of an image is proportional to the square root of the exposure time used. With an exposure time of 4 hours, the SNR values of the simulated observations would be approximately doubled.

5 Observing a Supernova Progenitor and a Star Cluster

In this section, a supernova progenitor is observed at the center of a star cluster. The magnitude of the progenitor comes from photometry data of the progenitor of supernova 2008bk [72]. The star cluster is generated using Scopesim's star cluster function, using inputs of: a total mass, cluster radius, and distance. The brightness and quantity of individual stars is determined by scopesim. The progenitor of supernova 2008bk has an apparent magnitude of 18.39 mag in the K_s band, 19.45 in the J band, and 20.02 in the Y band. The distance of the host galaxy is 3.5 Mpc [72]. These values were used to calculate the magnitude of the simulated progenitor at distances ranging from 3.5 Mpc to 94.5 Mpc. In each simulation, the progenitor is placed at the center of the cluster. The cluster masses used are 10^5 $M_\odot$ and 5×10^5 $M_\odot$; the cluster radius used in the simulations is 7 pc.

The purpose of these simulations is to explore the potential to resolve and identify a supernova progenitor from its neighbors. An anticipated advantage of using the ELT is its ability to resolve point sources with very small angular separations. In the previous section, it was found that the angular size of point sources (the FWHM) remains constant for varying magnitudes. Thus, the angular distance needed between two stars, for the stars to be resolved, is already known for each pixel scale in the K_s, J and Y bands. In this section, only the SCAO system was simulated. Each observation has an exposure time of 1 hr, and uses the parameters shown in table I.

The FWHM of point sources are summarized in Table III. In the J and Y bands, the FWHM of a point source is only one pixel, when the 4 mas pixel scale is used. Thus, at least two pixels (8 mas) should be between two point sources. At a distance of 94.5 Mpc, the angular size of the simulated star cluster is 30.5 mas. Given the

Pixel Scale	K_s	J	Y
4 mas	12	4	4
1.5 mas	13.5	6	6

Table III: The FWHM in mas of point sources for the K_s, J and Y bands, and the 4 mas and 1.5 mas pixel scales.

previously determined angular resolution of the optical system, the density of stars will far exceed the density at which individual stars could be resolved. Thus, 94.5 Mpc serves as a reasonable upper limit for the distances used in this exercise. This is nearly the distance to the Coma Cluster [73].

For each distance and cluster mass, the star cluster was observed both pre-supernova and post-supernova, (with and without the progenitor). The same difference-imaging technique used in the previous section is applied here. In this case, the reference image would be taken after the supernova has dissipated, and no light source appears at the location of the transient. The progenitor was also observed without the presence of the star cluster, so that the effects of including a star cluster in the observation can be compared to the results yielded by observing the progenitor without a star cluster. An example is shown in Figure 27, with a cluster mass of 5×10^5 $M_\odot$, a distance of 3.5 Mpc, in the Y band.

The simulated supernova progenitor, with photometric values taken from progenitor 2008bk, is substantially brighter than the stars generated by scopesim's star cluster function. For distances where the star cluster and progenitor are visible, and for cluster densities where stars can be resolved, the presence of the progenitor in the cluster is immediately evident. Scopesim's star cluster function does not allow the magnitudes of the stars to be set manually. Future analysis of simulated difference images would benefit from such customization, and the inclusion of subtracted stars

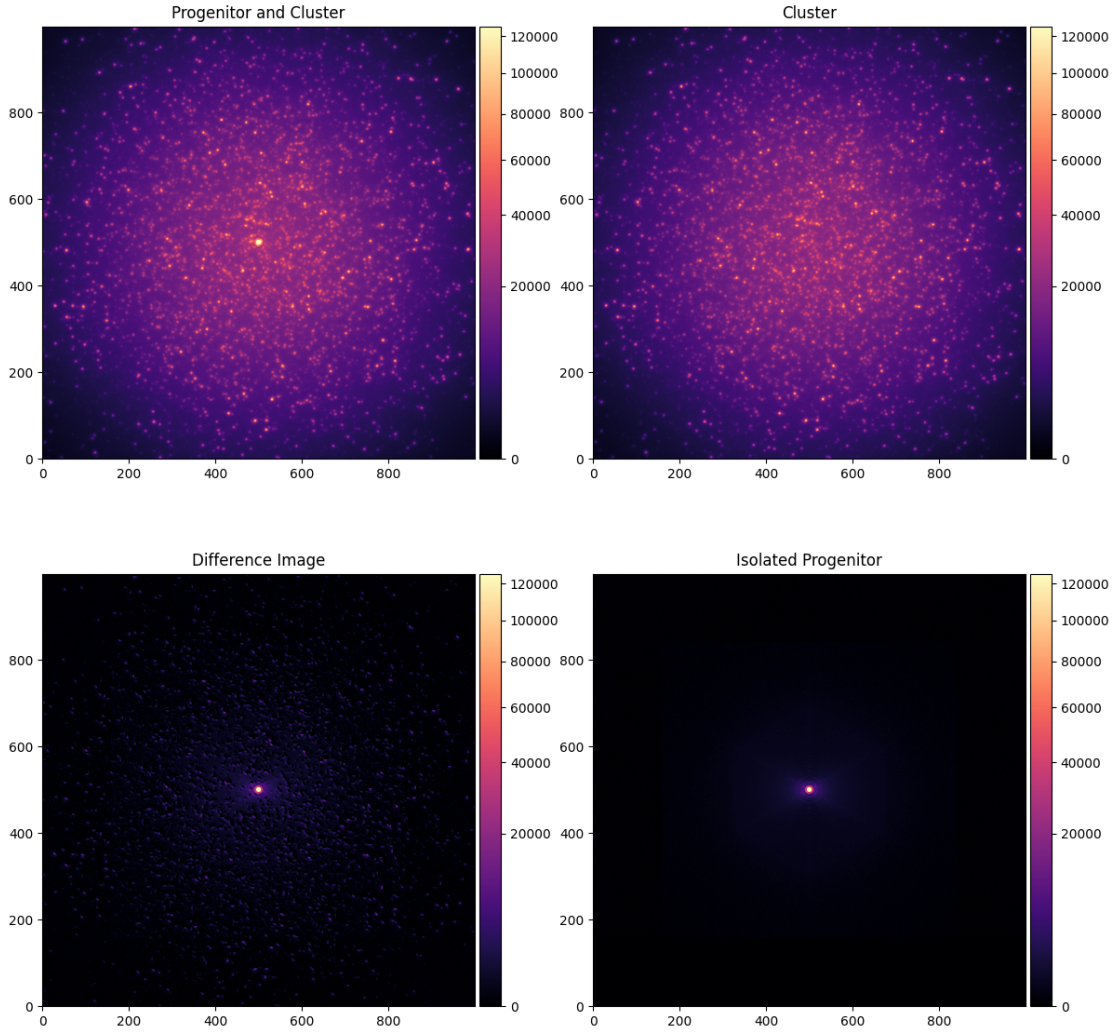

Figure 27: Upper left: the star cluster with a supernova progenitor at its center, upper right: the same star cluster without a progenitor, lower left: the difference image, lower right: the progenitor observed without a star cluster. Observed in the Y band, for 1 hour. The cluster distance is 3.5 Mpc, and the progenitor magnitude is 20 mag.

that are as bright, or brighter than the target object.

The difference image in Figure 27 appears significantly different from the image taken of an isolated progenitor observation. The subtraction of the star cluster has left remnants of light from the surrounding stars, increasing the noise in the image. This increase in noise may make it difficult to identify a progenitor in a difference

image. In the figures that follow in this section, the SNR of the difference images are plotted as a function of distance.

5.1 Results

Figure 28 shows the SNR vs distance of the supernova progenitor, with 10^5 $M_\odot$ and 5×10^5 $M_\odot$ star clusters subtracted from the frame, and with no star cluster subtracted, using the 4 mas and 1.5 mas pixel scales. When the 4 mas pixel scale is used, the mass of the star cluster makes a negligible contribution to the noise in the image. The presence of the star cluster decreases the SNR slightly from the values obtained without a star cluster in the observation. The SNR values are lower when the 1.5 mas pixel scale is used, however, the relative values between the points appear very similar. Regardless of pixel scale, the difference image of the progenitor has only a slightly lower SNR than what is obtained from a lone-progenitor observation.

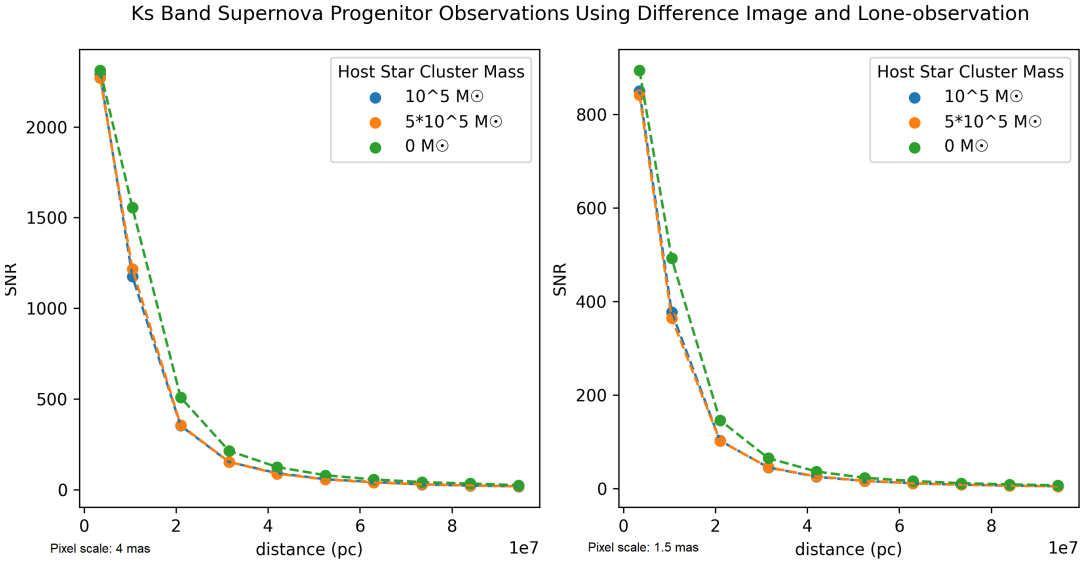

Figure 28: SNR vs distance of a supernova progenitor difference image in the K_s band. 4 mas pixel scale on the left, 1.5 mas pixel scale on the right.

Figure 29 shows the SNR vs distance of the supernova progenitor, with 10^5 $M_\odot$

and 5×10^5 $M_\odot$ star clusters subtracted from the frame, and with no star cluster subtracted, using the 4 mas and 1.5 mas pixel scales. When the 4 mas pixel scale is used, a small difference can be seen between the lower and higher star cluster masses. The subtraction of a higher mass yields a lower SNR for the progenitor difference image. When the 1.5 mas pixel scale is used, the star cluster mass makes significantly more of a difference in the SNR calculation. For distances less than 40 Mpc, the SNR value of the progenitor image with a 5×10^5 $M_\odot$ star cluster subtracted from the frame is nearly half of the SNR value obtained for an isolated star cluster.

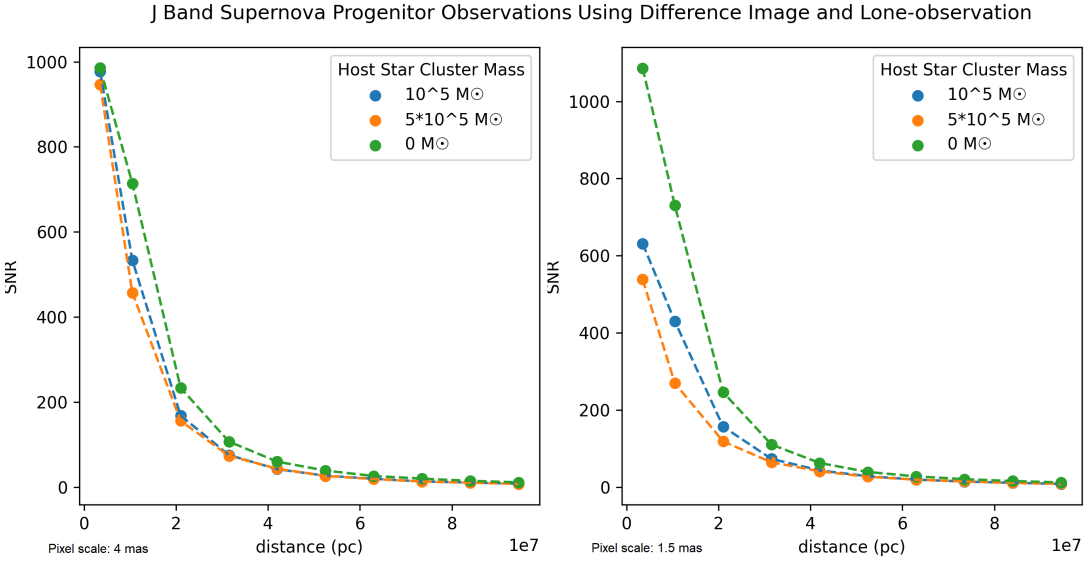

Figure 29: SNR vs distance of a supernova progenitor difference image in the J band, 4 mas pixel scale on the left, 1.5 mas pixel scale on the right.

Figure 30 shows the SNR vs distance of the supernova progenitor, with 10^5 $M_\odot$ and 5×10^5 $M_\odot$ star clusters subtracted from the frame, and with no star cluster subtracted. When the 4 mas pixel scale is used, the greatest difference in SNR values occurs at a distance of 10.5 Mpc. When the 1.5 mas pixel scale is used, the two smallest distances yield a drastic difference in the SNR values between the progenitor observed with no stars, and those that were observed in a cluster.

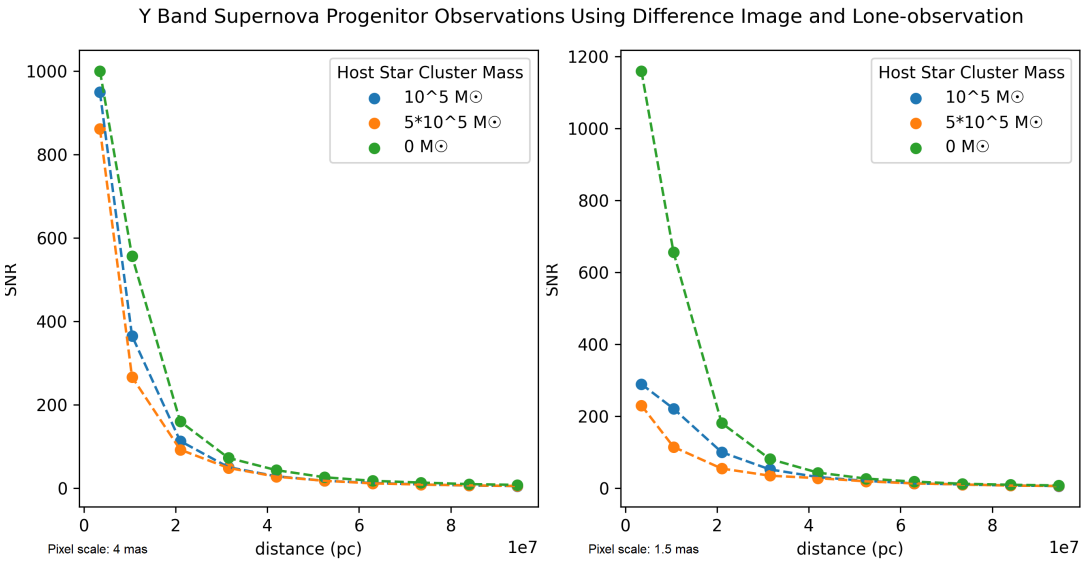

Figure 30: SNR vs distance of a supernova progenitor difference image in the Y band, 4 mas pixel scale on the left, 1.5 mas pixel scale on the right.

For each band, the effects on the SNR by the presence of the cluster decrease with increasing distance. As the distance increases, the magnitude of the stars decreases, causing them to contribute less to the noise in the difference image. There are some exceptions to this, where the difference in the SNR values increases from the distance of 3.5 Mpc to 10.5 Mpc. A possible reason for this is the increase in the density of stars in the area around the progenitor in the image. For larger distances, there are more stars within a small angular area around the progenitor, where the noise in the difference image is measured. The higher density of stars causes more noise. For distances beyond 10.5 Mpc, this effect is counteracted by the decrease in magnitude of the stars.

5.1.1 Detection Limit

A progenitor was considered detectable if the SNR of its image was at least 10. Table IV displays the greatest distances at which the progenitor was detected, and the SNR values of the progenitor image for those distances. In the K_s band, it appears that

the progenitor could have been detected at even greater distances using the 4 mas pixel scale; for each cluster mass, the SNR value at the largest distance tested was much higher than 10. For each band and pixel scale, the presence of a star cluster shortens the distance at which a progenitor could be detected.

Band	Pixel Scale	Cluster Mass ($M_\odot$)	Max. detection distance (pc)	SNR
K_s	4 mas	0	9.45×10^7	24
		10^5	9.45×10^7	18
		5×10^5	9.45×10^7	18
	1.5 mas	0	7.35×10^7	12
		10^5	6.3×10^7	11.5
		5×10^5	6.3×10^7	11.5
J	4 mas	0	9.45×10^7	11.5
		10^5	8.4×10^7	11
		5×10^5	8.4×10^7	11
	1.5 mas	0	9.45×10^7	12.5
		10^5	8.4×10^7	11
		5×10^5	8.4×10^7	11
Y	4 mas	0	8.4×10^7	10
		10^5	6.3×10^7	13
		5×10^5	6.3×10^7	12
	1.5 mas	0	8.4×10^7	10
		10^5	7.35×10^7	11
		5×10^5	7.35×10^7	11

Table IV: The maximum distance at which a progenitor was detected, for each band, pixel scale, and cluster mass, and the SNR of the progenitor image for that distance.

6 Discussion

6.1 Procedure Summary

The purpose of this research was to generate and study simulated astronomical observations, using the scopesim python package, and the properties of the ELT telescope and MICADO camera, to make an assessment of the feasibility of future research with the ELT. Scopesim was used to generate objects with various properties and to simulate observations with various observation parameters. The results were compared to determine which parameters produced the highest-quality images. The Strehl ratio, SNR and FWHM were obtained for a small selection of point source observations, to provide a quantitative comparison between observations, and to introduce these methods for further use. Supernovae were simulated with a host galaxy and observed at varying redshifts. The SNR, FWHM and Strehl ratio values of the supernovae are presented as a function of redshift, projected distance from the galaxy center, and the detector pixel scale. A supernova progenitor was simulated within a star cluster, with varying distances and cluster densities, to explore the ELT's potential to resolve a supernova progenitor from neighboring stars. The SNR of the progenitor is presented as a function of distance.

6.1.1 Scopesim Templates

The python package scopesim templates was used to simulate sets of stars, individual stars, star clusters, elliptical galaxies, a spiral galaxy, and point sources. These source objects enabled scopesim to successfully simulate observations. There are some source objects in scopesim templates that were found to not function correctly.

At the time that this research was conducted, the functions called "galaxy", "galaxy3d", "source from file" and "source from array" did not generate observable sources. Scopesim has since been updated, and some of these functions now work

as intended.

Scopesim templates also offers an empty sky function, so that an observation simulation can be run with no sources. The result of this observation is an image with only background radiation. This empty sky image is useful for reducing images of other observations. If the empty sky is observed with the same parameters as another source object, the empty sky frame can be used to subtract the background radiation from the image by subtracting the flux from the empty sky frame, pixel by pixel, from the science observation image.

The two AO systems, SCAO and MCAO were compared by using each to observe the same star cluster, with all other parameters kept the same. The star cluster was observed in the "Ks" band. The use of MCAO yielded a larger amount of background radiation, and the PSFs of the stars appeared to be wider.

The two pixel scales, 4 mas and 1.5 mas were compared in a similar manner as the AO comparison. In this case, a star cluster that is 15× more dense was used, to demonstrate the advantage of using a smaller pixel scale when observing an area with a dense population of light sources. When the 1.5 mas pixel scale is used, each pixel receives photons from a smaller area of the sky. Predictably, the image generated with the smaller pixel scale appears less bright. The 1.5 mas pixel scale is better at showing a dense set of light sources as separate points.

Scopesim's use of the atmospheric conditions: humidity, temperature, and air pressure, and the observation parameter airmass, were examined by changing each parameter to an extreme value, while keeping all other parameters at their default values. This was done to determine which parameters would yield drastic results with their variation, and which were considered negligible by scopesim. Increasing the airmass from 1.2 to 2.25 yielded a slight increase to the background radiation. Increasing the temperature from 7°C to 20°C yielded a drastic increase in the background radiation. Increasing the relative humidity from 0.1 to 1 showed no visible

changes to the image. Increasing the air pressure from 0.755 atm to 1 atm also showed no visible changes to the generated observation image. The shape of the PSF does not change with any changes in these parameters. These results should not be taken as a representation of how these conditions would affect a real observation. These results only definitively demonstrate the significance of modifying these parameters in a scopesim simulation.

The K_s, H, J, and Y bands were compared by simulating the same star cluster through each filter. The resulting images indicated that the PSF distribution is dependent on which filter is being used.

6.1.2 Introducing Analysis Tools

Three methods of analyzing a PSF were introduced, the FWHM, SNR, and Strehl ratio. The FWHM of a PSF was taken from a cross-section of the PSF. This cross section is presented along with the cross-section of an airy disk, in Figures 19 and 20. The FWHM of the cross-section is how the width of PSFs are quantified in this research.

To introduce the Strehl ratio, a point source of 22 mag was observed with each combination of AO systems and pixel scales, in the K_s, J and Y bands. The Strehl ratios of each image are plotted together for an easy comparison in Figure 21. Additionally, the Strehl ratio was used to assess how the airmass parameter is utilized by scopesim when generating a PSF. A point source was observed with a range of airmass values, and the Strehl ratio was plotted as a function of airmass, in Figure 22. The results show that the airmass has a negligible effect on the PSF produced by scopesim.

The SNR was introduced by observing a set of point sources with a range of magnitudes, calculating the SNR from each PSF, and plotting the SNR as a function of magnitude.

6.1.3 Supernovae And Galaxies

After introducing the PSF analysis tools, the goal was to simulate and study plausible observations of distant, redshifted supernovae, accompanied by a host galaxy. To select the magnitudes of the supernovae in the K_s, J and Y bands, the known properties of type Ia supernovae and astropy's cosmology package were used to calculate approximate apparent magnitudes of supernovae at various redshifts. The angular size of the galaxy, and the projected distance between the galaxy center and the supernova were also calculated using astropy's cosmology package. The supernova was simulated with three distances from the galactic center: 500 pc, 1 kpc, and 2 kpc. The host galaxy was simulated with and without the point source, and the flux from the host galaxy was subtracted from the image containing the supernova-galaxy system. Each difference image was used to obtain the SNR, FWHM, and Strehl ratio.

Of the three quantities that were calculated, only the SNR changed significantly with changes in redshift. The SNR varied slightly with changes in projected distance; in some instances, the SNR increased slightly with increased projected distance, in others, the opposite occurred. The 4 mas pixel scale consistently yielded higher SNR values than the 1.5 mas pixel scale. The Y band simulations had the highest SNR values, and the K_s band had the lowest.

The FWHM is invariant with redshift and projected distance. In the J and Y bands, the FWHM is 1 pixel, when the 4 mas pixel scale is used, and 4 pixels when the 1.5 mas pixel scale is used. In the K_s band, these values are 3 pixels and 9 pixels respectively.

The Strehl ratio changes very little with redshift and projected distance. In the K_s band, the Strehl ratios are within the range of 0.54-0.58. In the J band, the Strehl ratios were within the range of 0.21-0.27, with the 4 mas pixel scale yielding values slightly higher than when the 1.5 mas pixel scale was used. Observations in

the Y band yielded the lowest Strehl ratios: between 0.16 and 0.18; the Strehl ratios were slightly higher when the 4 mas pixel scale was used.

For each set of observations, the supernovae with the highest redshifts did not yield a detectable signal. In the K_s band, supernovae with redshifts less than 2 were detectable. In the J and Y bands, supernovae with redshifts less than 3 could be detected. The point source images with the lowest SNR values could not be used to compute valid FWHM and Strehl ratio values, and thus, these sources were considered entirely undetectable for the exposure time used.

6.1.4 Supernovae Progenitors and Star Clusters

A supernova progenitor was simulated with a star cluster, with varying cluster masses and distances, to investigate the potential for a supernova progenitor to be detected and resolved among a dense star population. The photometric parameters of the progenitor were taken from the progenitor of supernova 2008bk [72].

The angular size of a point source was already determined in the previous section, and thus, the limit of the density of point sources which can be resolved in an image is already known. Difference imaging was used to analyze observations which surpass this limit. For each distance and star cluster mass, the star cluster was observed both with and without the progenitor (pre and post supernova). The post-supernova frame was subtracted from the pre-supernova frame. The subtracted star cluster left substantial noise in each difference image. These difference images were compared to images of a supernova progenitor that was observed without a star cluster, to determine how much the additional noise would obscure the progenitor. The SNR was calculated for each progenitor image, and the SNR was plotted as a function of distance.

For each set of simulations, the SNR was consistently higher for progenitors that were observed without a star cluster. In some cases, the density of the star cluster

had no impact on the SNR of the difference image. The presence of a star cluster in the observation decreased the maximum distance at which the progenitor could be detected.

6.2 Analysis

6.2.1 The FWHM, Strehl Ratio, and SNR

For the central wavelengths of the K_s, J and Y bands, the diameters of the Airy disk are 27.9 mas, 8.0 mas, and 6.6 mas respectively. In the K_s band, the Airy disk diameter is approximately twice as large as the calculated FWHM of the PSF. The FWHM and Airy disk widths are correlative, but not directly comparable, because the radius of the Airy disk is defined at the distance of the first local minimum, and the FWHM is defined at the distance where the intensity is half of the central maximum. In the K_s band, the area of the PSF that has at least 50% of the intensity of the central maximum is within an area that is approximately half as wide as the Airy disk. In the J band, the ratio of the PSF FWHM and Airy disk diameter is also 0.5 when the 4 mas pixel scale is used; the ratio becomes 0.75 when the 1.5 mas pixel scale is used. In the Y band, the ratio of the PSF FWHM and Airy disk diameter is approximately 0.6 when the 4 mas pixel scale is used, and approximately 0.9 when the 1.5 mas pixel scale is used. These numbers indicate that the width of the PSF relative to the Airy disk increases with decreasing wavelength.

The Strehl ratio values were the highest when the K_s band was used, and the lowest when the Y band was used. These results are consistent with the comparison between FWHM and Airy disk values. For shorter wavelengths, the PSF is wider relative to the Airy disk, and therefore it is also shorter relative to the Airy disk.

The PSF is closer to the diffraction limit of the telescope at longer wavelengths because of the nature of AO corrections. The Fried Parameter (the length over which a wavefront changes phase by 1 radian) is smaller for shorter wavelengths, resulting

in a more spatially complex wavefront distortion. The coherence time (the amount of time that one arrangement of the deformable mirror yields a proper correction of the wavefront) is proportional to the Fried Parameter. Thus, for shorter wavelengths, AO corrections require greater spatial and temporal resolution.

ESO has an exposure time calculator (ETC) that, like scopesim, can be used to predict the SNR values of observations with the ELT [74]. For a redshift of $z = 1.84$, the apparent magnitude of the simulated supernova is 26.8 mag in the J band. When using the 4 mas pixel scale, the SNR of the supernovae were approximately 30. To compare this SNR with output from the ESO ETC, the parameters of the simulation were copied as closely as possible. Some of the parameters used in these simulations are not offered by the ESO ETC; the smallest pixel scale offered is 5 mas, and the AO modes offered are LTAO and GLAO. To compare the SNR of scopesim simulations using SCAO mode, LTAO was selected, as it is a system that also prioritizes mitigating on-axis turbulence, and works "almost as well as SCAO mode" [37]. Using these parameters, and airmass = 1.2, dit = 1 s, ndit = 3600, and the J band, the SNR value returned by the ESO ETC is 38.5.

This result is only 28% higher than the result found with the scopesim supernova simulations. Two obvious reasons that these values differ are the different pixel scales and the different AO systems that were used for each calculation. These parameters were chosen to be as similar as possible, but the results cannot offer a direct comparison. The noise may also be higher in the simulation of supernovae observations because of the observation and subtraction of a host galaxy. These SNR results are well within an order of magnitude of each other, indicating that these tools are decently consistent. This result is also consistent when the ETC is used to compare SNR values of dimmer point sources. For redshifts that are higher than 1.84, table V shows the SNR values obtained from the supernova simulations, SNR values obtained from the ETC, and SNR values obtained from the ETC using

a 4× longer exposure time. Each SNR obtained from the ETC is slightly higher than the respective SNR from the scopesim simulations. As expected, when the exposure time is 4× greater, the calculated SNR is approximately twice as high. The supernova with the highest redshift in the set, $z = 5.39$, would not be visible with 4 hours of exposure.

Redshift	Apparent Magnitude	SNR (Scopesim)	SNR (ESO ETC)	SNR (ESO ETC, 4h exposure)
2.58	27.5	15	20	40
3.77	29.7	1.8	2.7	5.3
5.39	32.6	0.1	0.18	0.37

Table V: A comparison of theoretical SNR values for dim point sources observed in the J band.

6.2.2 Comparison With Other Telescopes

When completed, the ELT will be the most powerful infrared telescope ever created. It will be more capable of observing faint, distant objects than the Hubble Space Telescope (HST), or the James Webb Space Telescope (JWST). The signal-to-noise calculators for each of these telescopes were used to compare the SNR calculations from Scopesim simulations of the ELT with the anticipated results of comparable observations made with the ELT.

The JWST is a space-based infrared telescope that was launched in 2021[75]. It has a 6.5m primary mirror, and an angular resolution of 0.07 arcsec [76, 77]. Much like the ELT, the JWST is intended to observe distant stars and galaxies. For near-infrared imaging with the JWST, the NIRCam instrument is used. The performace of the ELT and MICADO, and the JWST and NIRCam is compared in the following tables.

Table VI shows SNR values obtained from Scopesim simulations in the J band, and SNR values obtained from the JWST ETC for observations using the F115W filter. The filters used for each set of observations are close together on the electromagnetic spectrum, but are not exactly the same; the central wavelengths of the F115W filter and J filter are $1.15\mu m$ and 1.24 μm respectively. The detector parameters used with the JWST ETC are as follows: 9 groups per integration, 1 integration per exposure, 4 or 16 total dithers, and the medium 8 readout pattern [78, 79]. The total exposure times that were obtained with these parameters are 3779 s and 15117 s.

Redshift	Apparent Magnitude	SNR (ELT, Scopesim)	SNR (JWST)	SNR (JWST, 4h exposure)
1.84	26.8	30	24	48
2.58	27.5	15	13	26
3.77	29.7	1.8	1.8	3.6
5.39	32.6	0.1	0.1	0.25

Table VI: A comparison between SNR values from simulated ELT observations, and the JWST ETC, for observations of point sources in the J band. The exposure times used by the JWST ETC are 3779 s and 15117 s.

The SNR values for each set of 1h exposures indicate that the ELT will yield slightly better SNR values for comparable observations in the J band. These telescopes have similar sensitivity in the J band [80].

Table VII shows SNR values obtained from Scopesim simulations in the K_s band, and SNR values obtained from the JWST ETC for observations using the F210M filter. The central wavelengths of the F210W filter and J filter are $2.10\mu m$ and 2.16 μm respectively. The detector parameters used with the JWST ETC are identical to those previously discussed.

Redshift	Apparent Magnitude	SNR (ELT, Scopesim)	SNR (JWST)	SNR (JWST, 4h exposure)
1.4	26.7	12	22.9	45.8
1.7	27.6	5.2	10.5	21
2.97	28	3.4	7.4	14.8

Table VII: A comparison between SNR values from simulated ELT observations, and the JWST ETC, for observations of point sources in the K_s band. The exposure times used by the JWST ETC are 3779 s and 15117 s.

The calculated SNR values shown in table VII show that the JWST has greater sensitivity than the ELT in the K_s band. One reason that the SNR values may be lower for observations with MICADO is because of the width of the PSF relative to the pixel width. Simulations of point source observations in the K_s band have the widest PSFs of any simulations studied in this research; the FWHM of a PSF is 3 pixels when the 4 mas pixel scale is used. Having the intensity of the PSF spread over a larger number of pixels results in a PSF with a lower central maximum, and a lower SNR. The pixel scale of the JWST is 31 mas, much larger than MICADO's 4 mas pixel scale [81].

The HST is a space-based telescope that was launched in 1990 [82]. It has a 2.4 m primary mirror, and a spatial resolution of 0.13 arcsec [82, 83]. Throughout its decades of operation, the HST has facilitated many significant discoveries; it has helped astronomers map dark matter, identify black holes, study the births and deaths of stars, and much more [84]. For infrared imaging with the HST, the Wide Field Camera 3 (WFC3) is used. The performance of the ELT and MICADO and the HST and WFC3 is compared in table VIII. SNR values obtained form Scopesim simulations are presented along with SNR values obtained with the HST ETC, for the Y and J bands. The filters used by the HST ETC are F125W and F105Y, to

compare against the J and Y filters in the ELT, respectively.

J Band				
Redshift	Apparent Magnitude	SNR (ELT, Scopesim)	SNR (HST)	SNR (HST, 4h exposure)
1.84	26.8	30	7.9	16
2.58	27.5	15	4.2	8.4
3.77	29.7	1.8	0.5	1.1
5.39	32.6	0.1	0.04	0.07
Y band				
1.36	26	71	17	34
1.98	26.7	34	9.2	18
2.96	29	3.9	1.1	2.3
4.31	32	0.05	0.07	0.1

Table VIII: A comparison between SNR values from simulated ELT observations, and the HST ETC, for observations of point sources in the J and Y bands.

The SNR values shown in table VIII indicate that the ELT is substantially more sensitive than the HST in the J and Y bands. The SNR values of the ELT observation simulations are more than 3x higher than the values obtained for comparable HST observations.

Three metrics that can be used to compare the capabilities of telescopes are: detector sensitivity, spatial resolution, and spectral range. In the J band, the sensitivity of the ELT and JWST are similar. With the use of the ELT, rather than the JWST, in the J band, the distance at which a given supernova can be detected has increased only slightly. The advantage of using the ELT for such an observation is its superior spatial resolution. The pixel scale of the JWST is 31 mas – far wider

than any PSF obtained through simulations of the ELT [81]. The ELT has a greater capability of resolving a supernova from its host galaxy, or any other object with a small projected distance. In the K_s band, the sensitivity of the JWST is nearly twice as high as that of the ELT; the JWST can detect supernovae from a greater distance than the ELT.

The detector sensitivity of the HST is considerably less than the ELT and the JWST. The HST ETC predicts that an object with an apparent magnitude of 29.7 in the J band would have an SNR of 1.1 with a 4 hour exposure, making the HST insufficient for such an observation. The ELT ETC predicts that the SNR would be 5.3 for the same observation with the ELT. Additionally, the spatial resolution of the HST is poorer than that of both the ELT and JWST.

The range of wavelengths that will be observed with MICADO is 0.8μm to 2.4μm [32]. The ELT will have other instruments with other spectral ranges, making the total spectral range of the ELT 0.47μm to 2.45μm [85]. The spectral range of the JWST extends into the mid-infrared, to 28.5μm, far exceeding the range of the ELT [86]. The HST has a spectral range of 0.09μm to 2.5μm, covering visible and ultraviolet light that will not be observed with the ELT [87].

6.2.3 Use of Multiple Exposures and Positions

The simulation of multiple exposures, with random displacements of the telescope position, was used to make the noise in each exposure unique. This effort would be unnecessary if Scopesim's optical train included an optional random seed parameter for the generation of noise. The effect that is achieved by displacing the objects in the field of view could be achieved by changing the random seed with each use of the optical train. This would be more computationally efficient because a single source (or combination of sources) would be generated with scopesim templates and used in each exposure, instead of generating a new source, with a new position, for each

exposure.

However, the simulation of telescope movement between exposures would not be obsolete if a field-varying PSF is implemented. The PSF obtained from multiple exposures with varying telescope positions would be a linear combination of PSF distributions from each position used. A new python package called AnisoCADO is being developed; it will allow users to generate field-varying PSFs for the ELT [88]. If this package is made compatible with Scopesim, the dithering algorithm written for and used in this research would be a greater asset in future projects.

6.2.4 Difference Imaging

Difference imaging was used in Sections 4 and 5 to analyze observations of transient objects. The analysis of difference images offers a conservative outlook on what could be possible with the ELT. The difference images were made without varying observation parameters, such as exposure time, weather conditions, or airmass. The current version of scopesim uses one hard-coded PSF for each filter; the PSF does not change with any of these parameters. Therefore, no valid conclusions could be drawn about the viability of difference imaging with respect to varying observation conditions between each observation. Instead, this analysis shows what limitations should be expected with the most ideal set of pre- and post-transient observations, due to the additional noise that is present in difference images.

The analysis of difference images with scopesim could be greatly expanded in the future, with the implementation of a variable PSF distribution. With a PSF distribution that changes with atmospheric parameters and airmass, the simulation of pre- and post-transient observations should be done with varying observation parameters, to add greater complexity to the resultant difference image, and further assess the limitations of difference imaging with the ELT.

7 Conclusion

The purpose of this research was to use Scopesim to study the PSF of the ELT, and make a preliminary assessment of its potential use in imaging distant supernovae and supernova progenitors. In addition, Scopesim itself was studied to gauge the scope of its utility.

Scopesim has been found to have great potential as a tool for astronomers to use for planning their observations. Many source templates were tested (e.g. stars, star cluster, elliptical galaxy, spiral galaxy, and point source), along with many varying observation parameters. Multiple AO systems, pixel scales, filters, weather parameters, airmass values, exposure times, and detector sizes were tested.

At the time of this research, some of the source-template functions did not work correctly, such as the "source from file" and spiral galaxy functions. Variation in some observation parameters did not yield changes in output that align with expectations. The airmass parameter was found to have no effect on the Strehl ratio of a PSF. For each AO system and filter, one non-variable PSF is used by Scopesim. Scopesim cannot be used to investigate how any parameter other than the AO system or the filter will affect the shape of a PSF.

The case studies that were conducted with Scopesim found that the detection limits of point sources were in the range of 26 to 28 mag, with 1 hour exposures. The sensitivity of the detector was greater at shorter wavelengths. Although the PSF width is narrower at shorter wavelengths, the PSF is closer to the diffraction limit at longer wavelengths. A compromise can be made between the spatial resolution and the detection limit; using a larger pixel scale allows dimmer sources to be detected.

In general, difference imaging leaves a larger amount of noise in an image at shorter wavelengths. Difference imaging will be the most effective when the light being subtracted is diffuse. Point sources observed at longer wavelengths appear wider, resulting in an advantage when point sources are present in a reference im-

age: they can be subtracted with a smaller addition of noise. The effectiveness of difference imaging should be studied more extensively, with consideration for how varying observation parameters can affect a PSF.

References

[1] Zemax. What is a point spread function? https://support.zemax.com/hc/en-us/articles/1500005576562-What-is-a-Point-Spread-Function. (accessed 1/2025).

[2] Samuel J. Ling. *1.6 Huygens's Principle*, pages 26–30. OpenStax, Houston, Texas, 2016.

[3] Samuel J. Ling. *4.1 Single-Slit Diffraction*, pages 142–146. OpenStax, Houston, Texas, 2016.

[4] William Moebs Samuel J. Ling, Jeff Sanny. *University Physics Volume 3*. OpenStax College Rice University, 2016.

[5] J Tatum. *Optical Aberrations*, chapter 4. University of Victoria, 2021.

[6] The Editors of Encyclopaedia Britannica. *aberration*. Encyclopedia Britannica, 2016.

[7] Toshikazu Suzuki. An overview of full width at half maximum. https://www.pulstec.net/what-is-full-width-at-half-maximum/. (accessed 1/2025).

[8] Vladimir Sacek. Strehl ratio. https://www.telescope-optics.net/Strehl.htm. (accessed 6/2024).

[9] Vik Dhillon. Adaptive optics. http://www.vikdhillon.staff.shef.ac.uk/teaching/phy217/telescopes/phy217_tel_adaptive.html. (accessed 6/2024).

[10] Daniel R. Neal. *Shack-Hartmann sensor engineered for commercial measurement applications*, pages 140–160. SPIE Publications, 2005.

[11] Jim Schwiegerling and Daniel R Neal. *Historical development of the Shack-Hartmann wavefront sensor*. SPIE Publications, 2005.

[12] S.L. MEETOPTICS LABS. Wavefront sensors. https://www.meetoptics.com/academy/wavefront-sensors. (accessed 1/2025).

[13] Yahui Zhu, Ailing Tian, Hongjun Wang, and Bingcai Liu. Aspherical surface wavefront testing based on multi-directional orthogonal lateral shearing interferometry. *Sensors*, 24(23), 2024.

[14] Charlotte Z. Bond, Jean-François Sauvage, Noah Schwartz, Nicolas Levraud, Vincent Chambouleyron, Carlos Correia, Thierry Fusco, and Benoit Neichel. HARMONI at ELT: wavefront control in SCAO mode. In Laura Schreiber, Dirk Schmidt, and Elise Vernet, editors, *Adaptive Optics Systems VIII*, volume 12185, page 121851B. International Society for Optics and Photonics, SPIE, 2022.

[15] Roberto Ragazzoni. Pupil plane wavefront sensing with an oscillating prism. *Journal of Modern Optics*, 43(2):289–293, 1996.

[16] Enrico Pinna. *Study and Characterization of the Pyramid Wavefront Sensor for Co-phasing.* PhD thesis, UNIVERSITA DEGLI STUDI DI FIRENZE, 2004.

[17] Christophe Vérinaud. On the nature of the measurements provided by a pyramid wave-front sensor. *Optics Communications*, 233(1):27–38, 2004.

[18] Roberto Ragazzoni, Emiliano Diolaiti, and Elise Vernet. A pyramid wavefront sensor with no dynamic modulation. *Optics Communications*, 208(1):51–60, 2002.

[19] Chambouleyron, V., Fauvarque, O., Janin-Potiron, P., Correia, C., Sauvage, J-F., Schwartz, N., Neichel, B., and Fusco, T. Pyramid wavefront sensor optical gains compensation using a convolutional model. *AA*, 644, 2020.

[20] Richard Davies and Markus Kasper. Adaptive optics for astronomy. *Annual Review of Astronomy and Astrophysics*, 50(1):305–351, 2012.

[21] D Bonaccini Calia, Yan Feng, Wolfgang Hackenberg, Ronald Holzlöhner, Luke Taylor, and Steffan Lewis. Laser development for sodium laser guide stars at ESO. *The Messenger*, 139:12–19, 2010.

[22] R. Paschotta. Laser guide stars. https://www.rp-photonics.com/laser_guide_stars.html. (accessed 1/2025).

[23] David E. Reichle. Chapter 10 - the global carbon cycle and the biosphere. In David E. Reichle, editor, *The Global Carbon Cycle and Climate Change (Second Edition)*, pages 235–283. Elsevier, second edition edition, 2023.

[24] UCAR. The stratosphere. https://scied.ucar.edu/learning-zone/atmosphere/stratosphere. (accessed 12/2024).

[25] European Southern Observatory. ELT site. https://www.eso.org/sci/facilities/eelt/site/. (accessed 6/2024).

[26] European Southern Observatory. Timeline. https://elt.eso.org/about/timeline/. (accessed 6/2024).

[27] European Southern Observatory. Mirrors overview. https://elt.eso.org/mirror/. (accessed 6/2024).

[28] European Southern Observatory. M2 and m3 mirrors. https://elt.eso.org/mirror/M2M3/. (accessed 6/2024).

[29] European Southern Observatory. M4 mirror. https://elt.eso.org/mirror/M4/. (accessed 6/2024).

[30] European Southern Observatory. M5 mirror. https://elt.eso.org/mirror/M5/. (accessed 6/2024).

[31] European Southern Observatory. ESO - E-ELT Optical Design — eso.org. https://www.eso.org/sci/facilities/eelt/telescope/design/. (accessed 6/2024).

[32] European Southern Observatory. MICADO | ELT | ESO — elt.eso.org. https://elt.eso.org/instrument/MICADO/. (accessed 6/2024).

[33] Rodeghiero et al. The MICADO first light imager for the elt: preliminary design of the MICADO calibration assembly. page 323, 2018.

[34] Yann Clénet et al. The MICADO first-light imager for the elt: towards the preliminary design review of the MICADO-MAORY SCAO. In Laird M. Close, Laura Schreiber, and Dirk Schmidt, editors, *Adaptive Optics Systems VI*, volume 10703, page 1070313. International Society for Optics and Photonics, SPIE, 2018.

[35] Richard Davies, Veronika Hörmann, Sebastian Rabien, Eckhard Sturm, João Alves, Yann Clénet, Jari Kotilainen, Florian Lang-Bardl, Harald Nicklas, Jörg-Uwe Pott, Eline Tolstoy, Benedetta Vulcani, and Consortium. MICADO: The multi-adaptive optics camera for deep observations. *The Messenger*, 182:17–21, 2021.

[36] European Southern Observatory. MORFEO | ELT | ESO — elt.eso.org. https://elt.eso.org/instrument/MORFEO/. (accessed 6/2024).

[37] Adaptive optics | ELT | ESO — elt.eso.org. https://elt.eso.org/telescope/adaptiveoptics/. (accessed 6/2024).

[38] Jacques M. Beckers. Adaptive optics for astronomy: Principles, performance, and applications. *Annual Review of Astronomy and Astrophysics*, 31:13–62, 1993.

[39] F. Roddier. Adaptive optics: performance and limitations [invited]. In J. G. Robertson and William J. Tango, editors, *Very High Angular Resolution Imaging*, volume 158 of *IAU Symposium*, pages 273–281. Springer Netherlands, 1994.

[40] M. Le Louarn, N. Hubin, M. Sarazin, and A. Tokovinin. New challenges for adaptive optics: extremely large telescopes. *Monthly Notices of the Royal Astronomical Society*, 317(3):535–544, 2000.

[41] Enrico Cappellaro and Massimo Turatto. *Supernova Types and Rates*, page 199–214. Springer Netherlands, 2001.

[42] Rachel C. Wolf, Chris B. D'Andrea, Ravi R. Gupta, Masao Sako, John A. Fischer, Rick Kessler, Saurabh W. Jha, Marisa C. March, Daniel M. Scolnic, Johanna-Laina Fischer, et al. Sdss-ii supernova survey: An analysis of the largest sample of type Ia supernovae and correlations with host-galaxy spectral properties. *The Astrophysical Journal*, 821(2), 2016.

[43] K Taggart and D A Perley. Core-collapse, superluminous, and gamma-ray burst supernova host galaxy populations at low redshift: the importance of dwarf and starbursting galaxies. *Monthly Notices of the Royal Astronomical Society*, 503(3):3931–3952, 2021.

[44] D Koester and G Chanmugam. Physics of white dwarf stars. *Reports on Progress in Physics*, 53(7), 1990.

[45] Andrew M Low. The chandrasekhar limit: a simplified approach. *Physics Education*, 58(4), 2023.

[46] Ashley Villar. Classifying supernovae. https://astrobites.org/2016/12/02/classifying-supernovae/. (accessed 8/2024).

[47] Bo Wang and Zhanwen Han. Progenitors of type Ia supernovae. *New Astronomy Reviews*, 56(4):122–141, 2012.

[48] Dr. Melissa Graham. Supernova explosions. https://lco.global/spacebook/stars/supernova/. (accessed 8/2024).

[49] Duligur Ibeling and Alexander Heger. The metallicity dependence of the minimum mass for core-collapse supernovae. *The Astrophysical Journal*, 765(2):L43, 2013.

[50] Swinburne University of Technology. Type II supernova. https://astronomy.swin.edu.au/cosmos/t/Type+II+Supernova. (accessed 8/2024).

[51] Hans-Thomas Janka. Explosion mechanisms of core-collapse supernovae. *Annual Review of Nuclear and Particle Science*, 62(1):407–451, 2012.

[52] Las Cumbres Observatory. Redshift. https://lco.global/spacebook/light/redshift/. (accessed 8/2024).

[53] Edwin Hubble. A relation between distance and radial velocity among extragalactic nebulae. *Proceedings of the National Academy of Sciences*, 15(3):168–173, 1929.

[54] Tamara M. Davis. Superluminal recession velocities. In *AIP Conference Proceedings*. AIP, 2001.

[55] Peter J. Brown and Roming et al. The absolute magnitudes of type Ia supernovae in the ultraviolet. *The American Astronomical Society*, 721(2):1608–1626, 2010.

[56] The Asiago Database on Photometric Systems. 2mass. http://ulisse.pd.astro.it/Astro/ADPS/ADPS2/FileHtml/index_n021.html. (accessed 9/2024).

[57] Kieran Leschinski, Hugo Buddelmeijer, Oliver Czoske, Miguel Verdugo, Gijs Verdoes-Kleijn, and Werner W. Zeilinger. Scopesim: a flexible general purpose astronomical instrument data simulation framework in python. In Juan C. Guzman and Jorge Ibsen, editors, *Software and Cyberinfrastructure for Astronomy VI*, page 82. SPIE, 2020.

[58] A* Vienna. Scopesim. https://scopesim.readthedocs.io/en/stable/, 2019. (accessed 4/2024).

[59] Miguel Verdugo. Spectral libraries. https://spextra.readthedocs.io/en/latest/spectral_libraries.html, 2024. (accessed 4/2024).

[60] A* Vienna. Scopesim templates. https://scopesim-templates.readthedocs.io/en/latest/. (accessed 5/2024).

[61] L. Bottinelli, L. Gouguenheim, G. Paturel, and G. de Vaucouleurs. Hi line studies of galaxies. iii. distance moduli of 822 disk galaxies. *Astronomy and Astrophysics*, 56:381–413, 1984.

[62] Las Cumbres Observatory. Airmass limit. https://lco.global/documentation/airmass-limit/. (accessed 11/2024).

[63] Bo Xin, Željko Ivezić, Robert H. Lupton, John R. Peterson, Peter Yoachim, R. Lynne Jones, Charles F. Claver, and George Angeli. A study of the point-spread function in sdss images. *The Astronomical Journal*, 156(5):222, 2018.

[64] Steven W. Smith. *Statistics, Probability and Noise*, chapter 2, pages 11–34. California Technical Publishing, 2 edition, 1999.

[65] Craig Stark. Signal to noise: Understanding it, measuring it, and improving it (part 1). https://www.cloudynights.com/articles/cat/column/fishing-for-photons/signal-to-noise-understanding-it-measuring-it-and-improving-it-part-1-r189 (accessed 10/2024).

[66] David Harvey. 10.1: Signals and noise. https://chem.libretexts.org/Bookshelves/Analytical_Chemistry/Chemometrics_Using_R_(Harvey)/10%3A_Cleaning_Up_Data/10.1%3A_Signals_and_Noise. (accessed 10/2024).

[67] Gy. M. Szabó, K. Sárneczky, J. Vinkó, B. Csák, Sz. Mészáros, P. Székely, and Zs. Bebesi. Photometry of sn 2002bo with template image subtraction. *Astronomy & Astrophysics*, 408(3):915–919, 2003.

[68] Samaporn Tinyanont, R Ridden-Harper, R J Foley, V Morozova, C D Kilpatrick, G Dimitriadis, L DeMarchi, A Gagliano, W V Jacobson-Galán, A Messick, J D R Pierel, A L Piro, E Ramirez-Ruiz, M R Siebert, K C Chambers, K E Clever, D A Coulter, K De, M Hankins, T Hung, S W Jha, C E Jimenez Angel, D O Jones, M M Kasliwal, C-C Lin, R Marques-Chaves, R Margutti, A Moore,

I Pérez-Fournon, F Poidevin, A Rest, R Shirley, C S Smith, E Strasburger, J J Swift, R J Wainscoat, Q Wang, and Y Zenati. Progenitor and close-in circumstellar medium of type II supernova 2020fqv from high-cadence photometry and ultra-rapid uv spectroscopy. *Monthly Notices of the Royal Astronomical Society*, 512(2):2777–2797, 2021.

[69] Wenlei Chen, Patrick L. Kelly, Masamune Oguri, Thomas J. Broadhurst, Jose M. Diego, Najmeh Emami, Alexei V. Filippenko, Tommaso L. Treu, and Adi Zitrin. Shock cooling of a red-supergiant supernova at redshift 3 in lensed images. *Nature*, 611(7935):256–259, 2022.

[70] Y. Clénet, P. Baudoz, R. Davies, E. Tolstoy, and K. Leschinski. MICADO, the ELT first-light imager. In P. Di Matteo, O. Creevey, A. Crida, G. Kordopatis, J. Malzac, J. B. Marquette, M. N'Diaye, and O. Venot, editors, *SF2A-2019: Proceedings of the Annual meeting of the French Society of Astronomy and Astrophysics*, 2019.

[71] SCAO vs MCAO, PSF and fluxes behaviour in extended and star mode #157. https://github.com/AstarVienna/ScopeSim/issues/157. (accessed 9/2024).

[72] Justyn R. Maund, Seppo Mattila, Enrico Ramirez-Ruiz, and John J. Eldridge. A new precise mass for the progenitor of the type IIP sn 2008bk. *Monthly Notices of the Royal Astronomical Society*, 438:1577–1592, 2014.

[73] Bjarne Thomsen, William A. Baum, Mark Hammergren, and Guy Worthey. The distance to the coma cluster from surface brightness fluctuations. *The Astrophysical Journal*, 483(1):L37–L40, 1997.

[74] European Southern Observatory. Elt etc. https://www.eso.org/observing/etc/bin/gen/form?INS.NAME=ELT+INS.MODE=swimaging. (accessed 12/2024).

[75] NASA. About webb. https://science.nasa.gov/mission/webb/about-overview/. (accessed 12/2024).

[76] NASA. Webb's mirrors. https://science.nasa.gov/mission/webb/webbs-mirrors/. (accessed 12/2024).

[77] Stefanie N. Milam, John A. Stansberry, George Sonneborn, and Cristina Thomas. The james webb space telescope's plan for operations and instrument capabilities for observations in the solar system. *Publications of the Astronomical Society of the Pacific*, 128(959):018001, 2016.

[78] Space Telescope Science Institute. Understanding exposure times. https://jwst-docs.stsci.edu/understanding-exposure-times#gsc.tab=0. (accessed 12/2024).

[79] Space Telescope Science Institute. Nircam detector readout patterns. https://jwst-docs.stsci.edu/jwst-near-infrared-camera/

nircam-instrumentation/nircam-detector-overview/nircam-detector-readout-patterns#gsc.tab=0. (accessed 12/2024).

[80] Eckhard Sturm and Richard et al. Davies. The MICADO first light imager for the elt: overview and current status. In Joël R. Vernet, Julia J. Bryant, and Kentaro Motohara, editors, *Ground-based and Airborne Instrumentation for Astronomy X*, page 37. SPIE, 2024.

[81] Space Telescope Science Institute. Nircam imaging. https://jwst-docs.stsci.edu/jwst-near-infrared-camera/nircam-observing-modes/nircam-imaging#gsc.tab=0. (accessed 12/2024).

[82] NASA. Hubble space telescope. https://science.nasa.gov/mission/hubble/. (accessed 12/2024).

[83] J. Marinelli, M. Green. *Wide Field Camera 3 Instrument Handbook, Version 17.0*. Space Telescope Science Institute, 3700 San Martin Drive, Baltimore, MD, 2024.

[84] National Aeronautics and Space Association. Highlights of hubble's exploration of the universe. https://www.nasa.gov/wp-content/uploads/2017/01/highlights_of_hubbles_exploration_of_the_universe_0.pdf.

[85] European Southern Observatory. HARMONI | ELT | ESO — elt.eso.org. https://elt.eso.org/instrument/HARMONI/. (accessed 6/2024).

[86] Nasa. About the james webb space telescope. https://webbtelescope.org/contents/media/images/4168-Image#:~:text=Its%20four%20instruments%20provide%20wavelength,to%20a%20few%20hundred%20microns. (accessed 12/2024).

[87] Nasa. The electromagnetic spectrum (with hubble, webb, and spitzer highlights). https://webbtelescope.org/contents/media/images/4188-Image. (accessed 12/2024).

[88] Eric Gendron. Anisocado. https://anisocado.readthedocs.io/en/latest/, 2019. (accessed 11/2024).

[89] Eugene Hecht. *10.2.4 The Rectangular Aperture*, pages 483–485. Pearson Education, Harlow, UK, 2017.

[90] Eugene Hecht. *10.2.5 The Circular Aperture*, pages 488–492. Pearson Education, Harlow, UK, 2017.

A Derivation Of The Airy Disk

Consider the electromagnetic disturbance that arrives at a point P, from a tiny area dS, with dS being a piece of an arbitrarily sized and shaped aperture S. If dS is small enough to be considered a point source, and the light intensity $\mathcal{E}_A$ is constant across all of S, and point P is a distance r away from dS, and a distance R away from the center of S, then dE, the contribution to the disturbance at P from dS, is the real or imaginary part of

$$dE = \frac{\mathcal{E}_A}{r} e^{i(\omega t - kr)} dS \tag{3}$$

The strength of the electric field varies temporally and spatially due to its oscillation, with terms ωt and kr respectively, and is inversely proportional to the distance r from the source. The real and imaginary parts of the equation describe the same system, with the only difference being a phase shift [89].

In this system, the aperture S sits in the yz-plane, the normal vector points in the x-direction, the point P has coordinates (X,Y,Z), and dS has coordinates (0,y,z). To obtain a useful equation for the total disturbance E at point P, the value r should be expressed in terms of R,X,Y,Z,y and z, simplified, and substituted in equation 3. The value r can be expressed using the coordinates of dS and P:

$$r = [X^2 + (Y - y)^2 + (Z - z)^2]^{1/2} \tag{4}$$

The distance from the center of the aperture to P is

$$R = [X^2 + Y^2 + Z^2]^{1/2} \tag{5}$$

Equations 4 and 5 can be combined to obtain:

$$r = R \left[1 + \frac{y^2 + z^2}{R^2} - \frac{2(Yy + Zz)}{R^2} \right]^{1/2}. \tag{6}$$

This equation can be simplified if we consider the term $\frac{y^2+z^2}{R^2}$ to be negligible. This term can be omitted, given that y and z are within the bounds of S, and the height and width of S are much smaller than the distance between S and the image plane. Without this term, **Equation** 6 becomes

$$r = R \left[1 - \frac{2(Yy + Zz)}{R^2} \right]^{1/2} \tag{7}$$

Using the binomial theorem to expand **Equation** 7 and using the first two terms yields:

$$r = R \left[1 - \frac{Yy + Zz}{R^2} \right] \tag{8}$$

In **Equation** 3, the value r in the denominator can be substituted with R, because these terms are very similar in the far-field case, and this approximation will have a negligible effect on the result. The r term in the exponent determines the

phase of the oscillating electric field; this value is much more sensitive to changes in r, and shall be substituted with the value of r given in **Equation** 8. With these substitutions, the equation for the electromagnetic disturbance at P from light passing through S is

$$\tilde{E} = \frac{\mathcal{E}_A e^{i(\omega t - kR)}}{R} \iint_{\text{Aperture}} e^{ik(Yy+Zz)/R} dS \tag{9}$$

To find a function describing the interference pattern produced with a circular aperture, **Equation** 9 shall be evaluated for a system with a circular aperture S, having a radius of a. The circular symmetry of this system makes polar coordinates very convenient. Figure A1 shows the geometry of the circular aperture system.

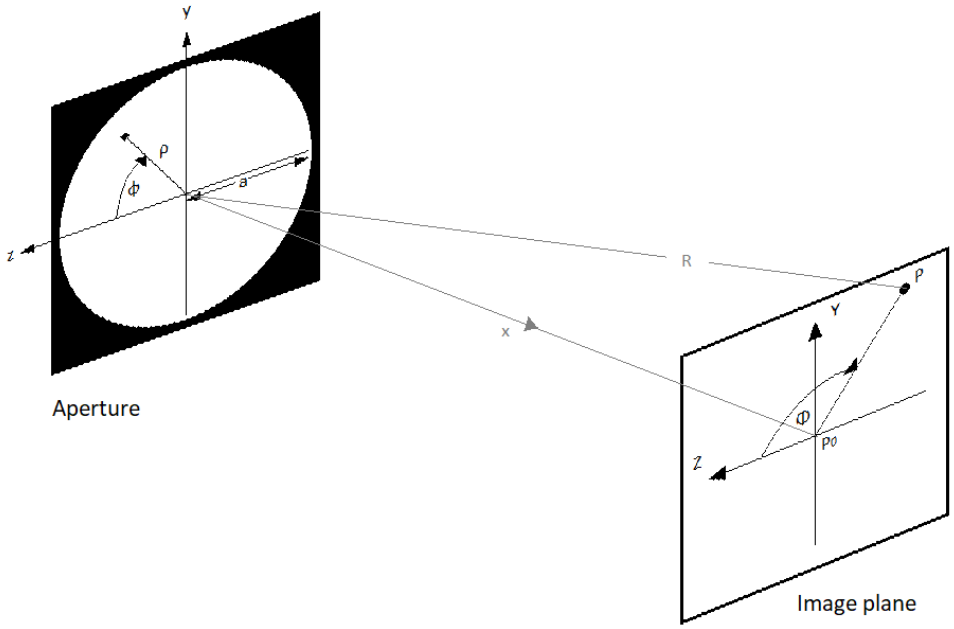

Figure A1: Geometry of a circular aperture and image plane. (Created by the author) [90]

The values y and z can be expressed in terms of their distance ρ from the center of S, and angle ϕ from the z-axis. The values Z and Y can be expressed in terms of their distance q from the center of the diffraction pattern P_0, and angle Φ from the zx-plane about the x-axis [90].

$$z = \rho \cos \phi \qquad y = \rho \sin \phi \qquad Z = q \cos \Phi \qquad Y = q \sin \Phi$$

The differential element dS in polar coordinates is

$$dS = \rho \, d\rho \, d\phi$$

Equation 9 can be rewritten as

$$\tilde{E} = \frac{\mathcal{E}_A e^{i(\omega t - kR)}}{R} \int_{\rho=0}^{a} \int_{\phi=0}^{2\pi} e^{i(k\rho q/R)\,\cos\,(\phi-\Phi)} d\phi \tag{10}$$

Given that the system has cylindrical symmetry, the value of $\tilde{E}$ on the image plane will be independent of Φ; this term can be set to $\Phi = 0$ to simply the equation.

The integral in **Equation** 10 that is to be integrated with respect to ϕ,

$$\int_0^{2\pi} e^{i(k\rho q/R)\,\cos\,\phi} d\phi$$

has the form of a Bessel function. It cannot be simplified to a more common function. In general, a Bessel function of order zero has the form

$$J_0(u) = \frac{1}{2\pi} \int_0^{2\pi} e^{iu\,\cos\,v} dv. \tag{11}$$

Equation 10 can be rewritten in terms of J_0, with $u = k\rho q/R$ and $v = \phi$.

$$\tilde{E} = \frac{\mathcal{E}_A e^{i(\omega t - kR)}}{R} 2\pi \int_0^a J_0\left(\frac{k\rho q}{R}\right) \rho\; d\rho \tag{12}$$

A Bessel function of a general order m has the form

$$J_m(u) = \frac{i^{-m}}{2\pi} \int_0^{2\pi} e^{i(mv + u\cos v)} dv \tag{13}$$

The first few Bessel functions are shown in Figure A2.

Bessel functions conveniently have a property known as a recurrence relation, which is expressed as

$$\frac{d}{du}[u^m J_m(u)] = u^m J_{m-1}(u) \tag{14}$$

The recurrence relation can be used to further simplify the equation for $\tilde{E}$. For m=1, equation **Equation** 14 yields

$$\int_0^u u' J_0(u') du' = u J_1(u) \tag{15}$$

with u' serving as a dummy variable.

The integral in **Equation** 12 can be modified with a new variable $w = (kq/R)\rho$. Now, $J_0(k\rho q/R) = J_0(w)$, $\rho = wR/kq$ and $d\rho = (R/kq)dw$. The new integral has the limit $w \in [0, kaq/R]$, and is expressed thusly:

$$\int_{\rho=0}^{\rho=a} J_0\left(\frac{k\rho q}{R}\right) \rho\; d\rho = \left(\frac{R}{kq}\right)^2 \int_{w=0}^{w=kaq/R} J_0(w) w\; dw. \tag{16}$$

Using **Equation** 15, the right side of **Equation** 16 can be expressed as:

$$\left(\frac{R}{kq}\right)^2 \left(\frac{kaq}{R}\right) J_1\left(\frac{kaq}{R}\right)$$

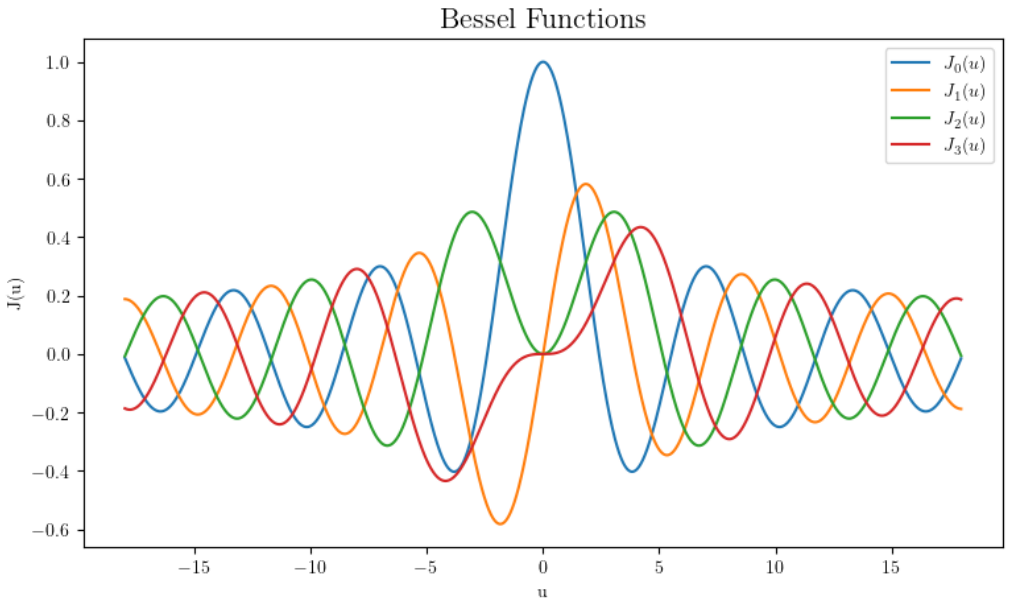

Figure A2: Bessel Functions of order 0, 1, 2, and 3.(Created by the author)

and the equation for $\tilde{E}$ becomes

$$\tilde{E} = \frac{\mathcal{E}_A e^{i(\omega t - kR)}}{R} 2\pi a^2 \left(\frac{R}{kaq}\right) J_1\left(\frac{kaq}{R}\right) \tag{17}$$

The irradiance at point-P is proportional to $\langle(\text{Re } \tilde{E})^2\rangle$, or $\frac{1}{2}\tilde{E}\tilde{E}*$ i.e,

$$I \propto \frac{2\mathcal{E}_A^2 A^2}{R^2} \left[\frac{J_1(kaq/R)}{kaq/R}\right]^2 \tag{18}$$

with the area of the aperture πa^a replaced with A.

To obtain an equation for irradiance in terms of the irradiance at the center of the image plane, I_0, the bracketed term in **Equation** 18 must be solved for $q = 0$, i.e, $\lim_{u\to 0} \frac{J_1(u)}{u}$ must be solved. From the recurrence relation shown in **Equation** 14, the following equation can be found for the case of $m = 1$.

$$J_0(u) = \frac{d}{du} J_1(u) + \frac{J_1(u)}{u} \tag{19}$$

Substituting $u = 0$ into **Equation** 11 yields the result $J_0(0) = 1$; substituting $u = 0$ and $m = 1$ into **Equation** 13 yields the result $J_1(0) = 0$. Instead of attempting to solve for $\lim_{u\to 0} \frac{d}{du} J_1(u)$ directly, L'Hospital's Rule can be utilized. L'Hospital's Rule tells us that

$$\lim_{u\to 0} \frac{dJ_1(u)}{du} = \lim_{u\to 0} \frac{J_1(u)}{u} \tag{20}$$

Taking the limit of **Equation** 19 as $u \to 0$ therefore yields

$$1 = \lim_{u\to 0} \frac{J_1(u)}{u} + \lim_{u\to 0} \frac{J_1(u)}{u} \tag{21}$$

making it obvious that $\lim_{u\to 0} \frac{J_1(u)}{u}$ and the bracketed term in **Equation** 18 are equal to $\frac{1}{2}$.

The irradiance can be expressed relative to I_0 by replacing the physical constants in **Equation** 20 with $I(0)$, and multiplying the term inside the brackets with a normalization coefficient so that $I = I(0)$ when $q = 0$. The result is

$$I = I(0)\left[\frac{2J_1(kaq/R)}{kaq/R}\right]^2. \tag{22}$$

The irradiance function can be rewritten as a function of the angular distance θ between the center of the image and point-P, with $\sin\theta = q/R$:

$$I = I(0)\left[\frac{2J_1(ka\,\sin\theta)}{ka\,\sin\theta}\right]^2 \tag{23}$$

Figure A3a shows the general shape of this function across one axis, and includes the relative values of local maxima and minima. Figure A3b shows how the irradiance function would appear on an image plane. The central peak is more than 50x higher than the next local maxima. It corresponds to a bright circular spot known as the Airy disk. The Airy disk is surrounded by a dark ring where $ka\sin\theta = 3.83$ and $I = 0$. Beyond the Airy disk are circular rings of relatively very low irradiance. For a given wavelength $\lambda = 2\pi/k$ and aperture diameter $D = 2a$, the angular distance between the center of the Airy disk and its outer edge is

$$\theta = \sin^{-1}\left(\frac{1.22\lambda}{D}\right). \tag{24}$$

The size of the Airy disk limits the physical resolution of an optical system. The Rayleigh criterion is a simple standard by which the potential to resolve two points can be assessed: it states that *two images are just resolvable when the center of the diffraction pattern of one is directly over the first minimum of the diffraction pattern of the other.* Therefore, **Equation** 24 is also the minimum angular separation between two resolvable points.

The aperture diameter of the ELT is 39m. The wavelengths of light that are detected by the camera MICADO range from $\lambda = 0.84\mu$m to $\lambda = 2.46\mu$m. The Airy disk radius of the ELT for each of these wavelengths is $\theta = 5.4$mas and $\theta = 16$mas respectively.

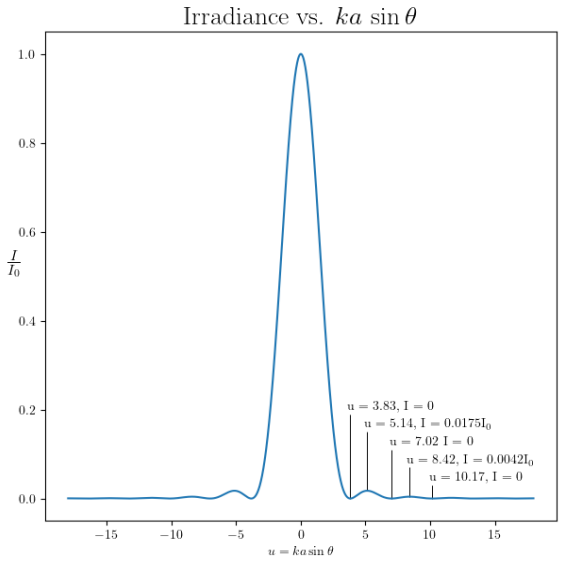

(a) The Airy pattern

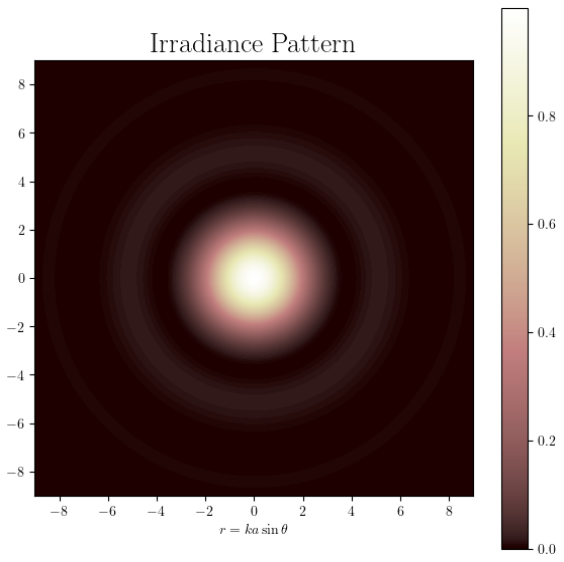

(b) The diffraction pattern from a point source passing through a circular aperture.

Figure A3: (Created by the author)